Journal of Geodesy (2026) 100:9
https://doi.org/10.1007/s00190-026-02031-2

ORIGINAL ARTICLE

Implications of phase information from GPS and GRACE(FO) for identifying GPS stations influenced by poroelastic deformation

Fei Lin[1,2] · Yu Sun[1,2] · Natthachet Tangdamrongsub[3] · Shuo Zheng[4] · Bao Zhang[5]

Received: 17 December 2023 / Accepted: 4 January 2026

Abstract

Phase information from vertical land motion observed by the Global Positioning System (GPS) and predicted by Gravity Recovery and Climate Experiment (GRACE) and GRACE Follow-On (GRACE-FO) has untapped potential for advancing hydrological and geophysical studies. After correcting for effects of glacial isostatic adjustment, non-tidal oceanic and atmospheric loading using existing models, GPS observations reflect both elastic deformation due to hydrological loading and poroelastic deformation in some aquifer regions. In contrast, GRACE(FO) data are sensitive only to mass changes and thus provide a good reference of elastic loading deformation. Over aquifer systems, discrepancies in the annual phase of vertical displacement between GPS and GRACE(FO) can therefore reveal where deformation is not explained by elastic loading alone but must also be influenced by poroelastic effects. In this study, we explore this phase difference as a diagnostic tool to identify GPS stations influenced by poroelastic deformation. By comparing the annual phases of GPS observation and GRACE(FO)-predicted elastic loading deformation, we establish a threshold-based criterion for identifying poroelastically influenced stations. We applied this method to the Central Valley of California and validated the results using in-situ well observations and a terrestrial water storage inversion based on GPS data. This phase-based identification method not only provides a simple, robust, and physically interpretable method for identifying GPS stations affected by poroelastic deformation but also highlights the broader potential of exploiting GPS and GRACE(FO) phase information in hydrological and geophysical studies.

Keywords Poroelastic deformation · Load-induced crustal elastic deformation · Terrestrial water storage · Aquifer system

1 Introduction

Monitoring terrestrial water storage (TWS) is essential for understanding environmental changes and their impact on human societies (Masson-Delmotte et al. 2021; Vereecken et al. 2022; Zhao et al. 2022). Mass redistributions such as ice melt, snow, water, and atmospheric changes play a significant role in shaping the Earth's surface and influencing the evolution of its interior (Humphrey et al. 2023; Zhang et al. 2023). In the context of climate change, with extreme droughts occurring more frequently, understanding these redistributions is crucial for managing water resources, particularly in regions facing water shortages (Gamelin et al. 2022; Jiang et al. 2021; Zhang & Yuan 2020; Zhu et al. 2024).

TWS can be monitored by the GRACE and GRACE Follow-On (GRACE-FO) missions, which provide global TWS measurements. However, due to their coarse spatial (300–500 km) and monthly temporal resolution, these data

✉ Yu Sun
jade.yusun@outlook.com

1 Key Lab of Spatial Data Mining and Information Sharing, Ministry of Education, Fuzhou University, Fuzhou, China

2 National and Local Joint Engineering Research Center of Satellite Geospatial Information Technology, Fuzhou University, Fuzhou, China

3 Water Engineering and Management, Faculty of Infrastructure, Asian Institute of Technology, Pathum Thani, Thailand

4 State Key Laboratory of Geodesy and Earth's Dynamics, Hubei Luojia Laboratory, Innovation Academy of Precision Measurement of Science and Technology, Chinese Academy of Sciences, Wuhan, China

5 School of Geodesy and Geomatics, Wuhan University, Wuhan, China

Published online: 01 February 2026

are less effective at capturing localized hydrological processes (Argus et al. 2014; Carlson et al. 2022; Humphrey et al. 2023). Components of TWS, such as groundwater storage (GWS), can be inferred using in-situ well measurements, which provide accurate local data on groundwater levels. Despite their accuracy, these measurements are limited by sparse geographical coverage and high maintenance costs (Renu & Pramada 2023). Global Positioning System (GPS), although not originally designed for monitoring mass changes, records surface displacements caused by loading and unloading processes (Ferreira et al. 2019; Lenczuk et al. 2023; Wang et al. 2017; White et al. 2022), allowing it to estimate TWS changes at a much higher spatial resolution, particularly in areas with dense GPS networks, such as the western United States (Amos et al. 2014; Argus et al. 2014; Zhong et al. 2020). For instance, Borsa et al. (2014) used data from 771 GPS stations to estimate a total mass loss of about 2.5 million tons in the western United States during the intense drought of 2013–2014. Similarly, Argus et al. (2014, 2017) analyzed a denser GPS network (922/1276 stations) over California, revealing significant seasonal TWS variations equivalent to 0.6 m of water thickness in the Klamath mountains, and a total mass loss of 45 ± 21 km^3 in the Sierra Nevada region during the 2011–2015 dry period. These examples demonstrate the ability of GPS to resolve TWS changes at spatial scales of tens of kilometers, which surpasses the resolution of GRACE(FO).

However, GPS stations often record signals from multiple sources, including both loading signals (e.g., due to hydrological mass changes) and non-loading signals such as poroelastic deformation, which results from changes in aquifer pore pressure due to groundwater fluctuations (Galloway & Burbey 2011; Ojha et al. 2018; Razeghi et al. 2022; Smith et al. 2017). These poroelastic deformation in GPS time series can lead to erroneous estimates of TWS if not properly accounted for. To accurately estimate TWS changes, one strategy is to, respectively, model both poroelastic deformation and elastic loading deformation and integrate them into a joint inversion framework (Carlson et al. 2024), or to isolate the elastic component from the GPS data (Kang & Knight 2023; Larochelle et al. 2022). For instance, Larochelle et al. (2022) applied a blind-source separation framework that combines Independent Component Analysis (ICA) of groundwater-level time series with residual GPS displacement (after removing GRACE(FO)-predicted elastic loading deformation). By projecting the GPS residuals onto ICA-derived groundwater components, they extracted spatially resolved poroelastic deformation fields and inferred aquifer mechanical properties. Another approach was introduced by Kang and Knight (2023), who leveraged the spatiotemporal characteristics of InSAR time series to distinguish poroelastic from elastic signals. Their method used k-means clustering and Principal Component Analysis (PCA) to classify deformation patterns based on seasonal phase behavior. This allowed them to isolate poroelastic signals in California's Central Valley without using GRACE(FO) or groundwater data. Although their approach was demonstrated using InSAR, the underlying principle of identifying consistent differences in seasonal timing may also be applied in regions with dense GPS station coverage. However, their method assumes that elastic loading deformation exhibits only seasonal characteristics for separation, which does not align with the long-term characteristics of mass loading effects. Most recently, Carlson et al. (2024) proposed a hybrid joint inversion method that integrates GPS, GRACE(FO), and InSAR data. This method combines geometrical and gravitational-based observations of TWS change and explicitly models both elastic and poroelastic deformation using different Green's functions, representing a significant advancement in TWS inversion methodology. While these methods offer improved accuracy, they typically require dense observational networks and detailed supporting data such as aquifer properties or InSAR measurements, making them challenging to apply at the continental scale or in aquifer systems where aquifer property data are lacking.

Another more conservative and widely adopted strategy is to identify and exclude GPS stations contaminated by poroelastic deformation from the inversion process (Argus et al. 2014; 2017; Carlson et al. 2022; Hammond et al. 2018). One common approach is to examine long-term subsidence trends, under the assumption that subsidence trend indicates groundwater depletion and opposite to the elastic loading direction and thus poroelastic influence (Argus et al. 2014; 2017; Carlson et al. 2022; Hammond et al. 2018). For example, Carlson et al. (2022) excluded GPS stations showing strong subsidence trend in California's Central Valley aquifer areas, especially those with rates greater than 2.5 mm per year. Other signs of poroelastic influence, such as unusually large seasonal signals and uplift that peak during the aquifer recharge period from March to May, have also been used to screen out affected stations (Argus et al. 2014; 2017; Carlson et al. 2022; Hammond et al. 2018). However, recent study has shown that long-term groundwater depletion does not always lead to long-term surface subsidence and may even cause uplift (Overacker et al. 2022), in which case this method may ineffective. Another approach is to compare individual stations to their regional neighbors, assuming that poroelastic deformation is spatially localized. Outlier stations—those whose displacement signals differ significantly from nearby stations—are flagged as contaminated (Jiang et al. 2017; Johnson et al. 2021; Lau et al. 2020). Carlson et al. (2024) further proposed using time series anti-correlations between GPS-observed surface deformation and that inferred from GRACE(FO) data, with poorly correlated stations are considered to be affected by non-hydrologic

loading processes, including poroelastic deformation. However, it is important to note that these screening strategies may be affected by other non-hydrologic signals in GPS time series, such as tectonic motion, volcanic activity, oil and gas extraction, glacial isostatic adjustment (GIA), and slow-moving landslides (e.g., Argus et al. 2017; Carlson et al. 2022; Razeghi et al. 2022). These non-hydrologic processes primarily influence the long-term trends of GPS time series, potentially leading to misclassification when using trend-based or correlation-based criteria. Consequently, caution is required when interpreting long-term subsidence or low correlation values as diagnostic indicators of poroelastic deformation.

Despite progress in mitigating poroelastic contamination in GPS-based hydrological studies, one key diagnostic signal remains underutilized: the seasonal phase of vertical displacements. Phase information offers a unique opportunity to identify GPS stations affected by poroelastic deformation, particularly when leveraged alongside GRACE(FO)-derived estimates of surface displacement that are sensitive only to mass changes. In this study, we investigate the utility of seasonal phase information as a diagnostic tool for detecting poroelastically affected GPS stations. We do not attempt to separate poroelastic and elastic loading signals at each station but focus on identifying stations dominated by either of them. By comparing the seasonal phase of vertical displacements observed by GPS with those inferred from GRACE(FO)-based elastic loading models, we develop a simple and physically interpretable method to identify GPS stations affected by poroelastic deformation.

2 Materials and methodology

2.1 Datasets

In this section, we briefly introduce the main datasets, GPS and GRACE(FO). We also mention two auxiliary datasets that are used in validation, including two hydrology models and in-situ well measurements.

2.1.1 GPS data

We utilized vertical land motion time series in new IGS20 framework from the Nevada Geodetic Laboratory (NGL) (Blewitt & Hammond 2018). Unlike the previous IGS14 solution, the IGS20 solution incorporates seasonal geocenter motion (degree-1), thereby reducing the aliasing of geocenter signals into GPS-observed vertical displacements. By modeling these effects, IGS20 solution offers a more physically consistent time series for analyzing vertical land motions driven by surface mass redistribution. We exclude stations with observations data spanning less than 1 year. Then the data were corrected for solid Earth tides, polar motion, and ocean tide loading (Blewitt et al. 2013; Petit & Luzum 2010), with a focus on seasonal deformation driven by hydrological loading. Data preparation involved removing outliers using the interquartile range method (Langbein & Bock 2004; Li et al. 2023; Razeghi et al. 2022) and correcting for atmospheric and non-tidal ocean loading using GFZ products (Dill & Dobslaw 2013; Martens et al. 2020) (Figure S2, accessed on 15 September 2023, http://rz-vm115.gfz-potsdam.de:8080/repository). The resulting time series were assumed to reflect seasonal terrestrial water storage (TWS) changes through the annual-harmonic terms.

2.1.2 GRACE(FO) data

We used GRACE(FO) gravity fields provided by multiple research institutions, including the Jet Propulsion Laboratory (JPL) (Wiese et al. 2018), Center for Space Research (CSR) (Save et al. 2016), and Goddard Space Flight Center (GSFC) (Loomis et al. 2019). Our analysis focused on level-3 "mascon" solutions, which were pre-corrected for low-degree coefficients (degree-1, C_{20} and C_{30}) (Loomis et al. 2020; Sun et al. 2016; Swenson et al. 2008) and GIA signals (Peltier et al. 2015). These mascon solutions are free from north–south stripe errors due to the regularization strategies applied (Wang et al. 2020; Wiese et al. 2016), so do not require additional post-processing steps and can be used directly. We converted the mascon fields to spherical harmonics to calculate vertical elastic loading deformation using Eq. 2. In this study, we mainly show the results based on JPL mascon solution named TELLUS_GRAC-GRFO_MASCON_CRI_GRID_RL06.1_V3, but results from other mascon solutions were consistent (Figures S5, S6).

2.1.3 Hydrological model

The WaterGAP Global Hydrology Model (WGHM) (Müller Schmied et al. 2021) is a comprehensive model developed by the University of Frankfurt, Germany, for global water resources analysis and forecasting. It integrates a global hydrological model with a variety of water use models, including those for irrigation, livestock, thermal power plants, and domestic households. WGHM not only calculates the long-term average water resources of specific countries or river basins, but also simulates all the components of TWS, excluding glaciers. These components include soil water, runoff, groundwater recharge, surface snowpack, and surface water storage (e.g., vegetation canopy water, rivers, lakes, reservoirs, and wetlands). The model provides data at a spatial resolution of 0.5° and a temporal resolution of one month, allowing for detailed analysis of water storage changes across different regions and time periods.

2.1.4 Land surface model

The TWS estimates are generated using the Noah-Multi-Parameterization (Noah-MP) (Niu et al. 2011) land surface model (LSM) at a 0.05-degree resolution (approximately 5 km) from 2002 to the present. These data are part of the Regional TWS Simulation at 5 km (RTWS5) product, provided by the Asian Land Information for Climate and Environmental Laboratory (ALICE-LAB; https://www.alice-lab.com). The Noah-MP LSM is designed to simulate land–atmosphere exchanges, including processes such as soil moisture, snow accumulation, vegetation dynamics, and energy balance. It includes multiple parameterization options, allowing for the simulation of various physical processes like groundwater, canopy resistance, and snow dynamics, providing flexibility for different environmental conditions. Noah-MP simulates TWS by incorporating key water storage components, such as soil moisture across four layers, snow water equivalent, canopy storage, and groundwater. The model is driven by meteorological forcing data from the ECMWF Reanalysis Version 5 (ERA-5) and operates at an hourly timestep, producing TWS outputs at a monthly scale to match the temporal resolution of GRACE(FO) data. Detailed information about the parameter configurations and model physics is available at https://www.alice-lab.com.

2.1.5 Well measurements

In-situ well observations provide accurate data on groundwater level fluctuations, which can be used to infer changes in groundwater storage (GWS) in the study area. For this study, well data were retrieved from the United States Geological Survey (USGS) National Water Information System database (https://waterdata.usgs.gov/nwis/dv/?referred_module=gw, accessed on September15, 2023). To align with the temporal coverage of GRACE(FO) and GPS data, we selected well sites with records from 2002 to the end of 2023, requiring at least 3.5 years of data and a minimum of 10 months of data per year.

2.2 Methodology

Elastic deformation of the Earth's crust is primarily caused by hydrological loads, such as water and snow, and occurs over large spatial scales. When these loads increase (e.g., during snow accumulation or heavy precipitation), the additional weight causes the crust, and therefore the surface, to subside (Fig. 1a). Conversely, when the load decreases (e.g., during snowmelt or drought), the crust rebounds, causing surface uplift (Fig. 1b). GPS stations, located at the Earth's surface, observe these vertical displacements, which predominantly reflect elastic loading deformation in regions without significant aquifer systems (Farrell 1972; Heki & Jin 2023).

In contrast, poroelastic deformation is driven by changes in pore pressure within aquifers. Variations in hydraulic head—caused by processes such as groundwater pumping, recharge, or head changes in connected aquifer systems—lead to changes in pore pressure (Biot & Willis 2021; Wilson & Gorelick 1996). A decrease in hydraulic head reduces pore pressure, increasing the effective stress on the aquifer skeleton and causing compression of the porous medium, which can result in surface subsidence (Fig. 1d) (Biot 1956; Wilson & Gorelick 1996). Conversely, an increase in hydraulic head raises pore pressure, reduces effective stress, and may cause surface uplift as the aquifer expands (Fig. 1c). The magnitude and spatial pattern of this deformation depend on the compressibility of both the fluid and the solid matrix (Biot & Willis 2021; Ojha et al. 2018). Unlike elastic loading deformation, poroelastic deformation is more localized, occurring not from any but only from confined or semi-confined aquifers (Razeghi et al. 2022). Because poroelastic deformation typically occurs in the opposite direction to the elastic loading deformation, it creates a more complex surface motion (Argus et al. 2017; Carlson et al. 2020; White et al. 2022). GPS stations in these regions, therefore, record a combination of both effects. Although poroelastic deformation occurs on a smaller spatial scale, its magnitude can exceed that of elastic loading deformation, especially in aquifer systems with thick clay aquitards and with heavy groundwater extraction (Argus et al. 2017; Carlson et al. 2020; Larochelle et al. 2022; White et al. 2022).

Our method focuses on analyzing the phase difference between the vertical land motion recorded by GPS and the elastic loading deformation inferred from GRACE(FO) data. GRACE(FO) measures mass changes across the Earth's vertical column, providing a reliable estimate of elastic loading deformation in the broader region. By comparing the phase of the GPS displacement time series to the phase of elastic deformation inferred from GRACE(FO), we can identify GPS stations affected by poroelastic deformation. Stations with significant phase differences are flagged as being influenced by localized poroelastic effects. Therefore, we only need to examine the absolute phase difference to determine if a site is affected by poroelastic deformation.

After preprocessing the GPS vertical displacement data (Sect. 2.1), we applied a least-squares fitting model that accounts for offsets, long-term trends, seasonal variations,

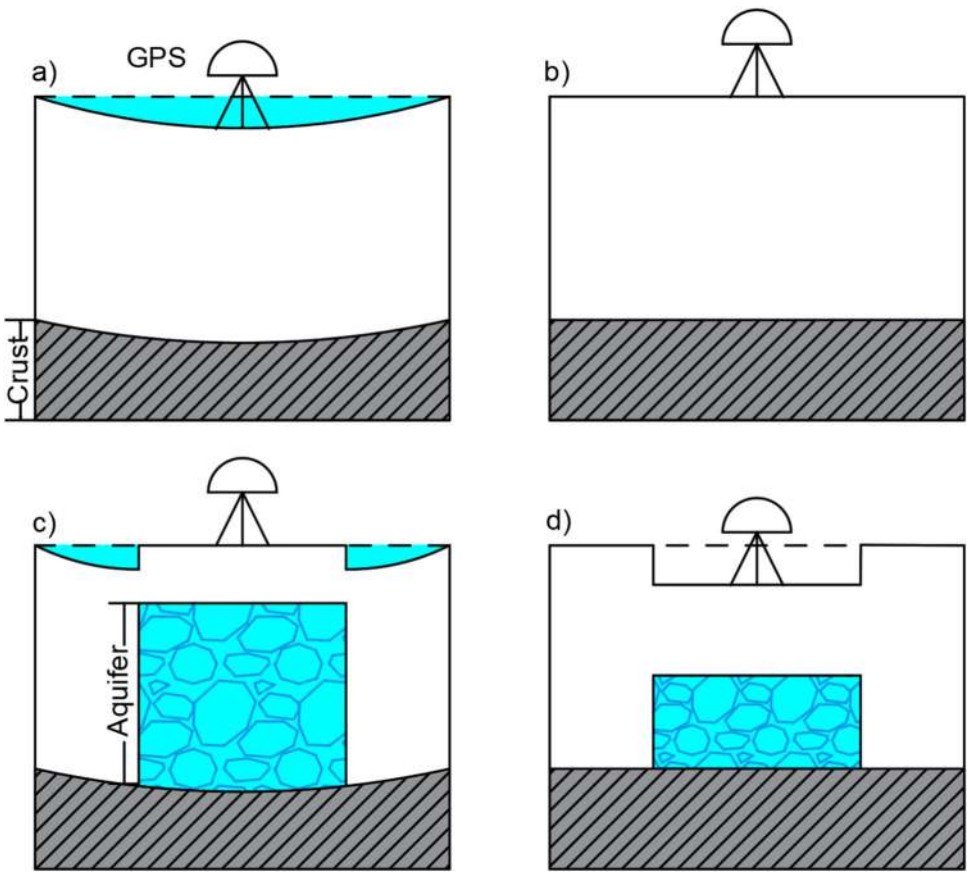

Fig. 1 A schematic diagram showing how a GPS station responds to different loading scenarios. Panels (**a**) and (**b**) show how a GPS station would react to surface loading and unloading; panels (**c**) and (**d**) show how a GPS station would react to groundwater recharge and over-depletion of an aquifer

and other factors like seismic jumps and post-seismic relaxation (Amos et al. 2014):

$$x(t_i) = b + \nu t_i + \sum_{j=1}^{2}\left[S_j \sin(2\pi j t_i) + C_j \cos(2\pi j t_i)\right] + \sum_{m=1}^{k} E_m H(t_i - t_m) + \sum_{n=1}^{l}\left[H(t_i - t_n) A_n log(1 + \frac{t_i - t_n}{\tau})\right] + \varepsilon_i, \quad (1)$$

where b is the offset, ν is the long-term velocity, and t_i is the daily epoch in decimal year. C_j and S_j represent the amplitude of annual ($j = 1$) and semiannual components ($j = 2$); H is the Heaviside function; E_m is the coseismic jump at epoch t_m; A represents the amplitude of post-seismic motion; and t_n represents the start time of the post-seismic transient. The relaxation time τ of the post-seismic transient is assumed to be 67 days (Zheng et al. 2023). Errors are represented by ε_i. Note that seismic events affecting each GPS station are usually provided by the data centers providing estimates of GPS position.

For GRACE(FO) data (Sect. 2.1), we estimated elastic loading deformation following Wahr et al. (1998):

$$U(\theta, \lambda) = \frac{3}{\rho}\sum_{l,m}\frac{h_l}{1+2l} P_{lm}(\cos\theta) \times \left[C_{lm}\cos(m\lambda) + S_{lm}\sin(m\lambda)\right], \quad (2)$$

where ρ is the average density of the Earth, and $P_{lm}^{/phantomi}$ is the regularized Legendre function of degree l and order m. C_{lm} and S_{lm} are the spherical harmonic coefficients of the equivalent water height, θ and λ are the latitude and longitude, respectively. h_l denotes the elastic loading Love number of degree l. We also compared these deformation results with those obtained by convolving surface mass changes with load Green's functions and found no significant differences (Figure S1).

The vertical deformation from GRACE(FO) was modeled using a simplified equation that excludes jumps and post-seismic relaxation, as GRACE(FO) does not observe these phenomena:

$$x(t_i) = b + \nu t_i + \sum_{j=1}^{2}\left[S_j \sin(2\pi j t_i) + C_j \cos(2\pi j t_i)\right] + \varepsilon_i. \quad (3)$$

The annual seasonal phase φ for both GPS and GRACE(FO) deformation time series can be calculated as follows:

$$\varphi = arctan\left(\frac{S_1}{C_1}\right) \cdot \frac{365}{2\pi} \tag{4}$$

and the uncertainty of the phase σ_φ can be computed using

$$\sigma_\varphi = \frac{365}{2\pi} \cdot \sqrt{\frac{{C_1}^2\sigma_{S_1}^2 + {S_1}^2\sigma_{C_1}^2}{({S_1}^2 + {C_1}^2)^2}}, \tag{5}$$

where σ_{S_1} and σ_{C_1} represent the uncertainty of S_1 and C_1, respectively.

2.3 Determination of the threshold

We quantified the phase differences between GPS and GRACE(FO) deformation time series. In regions without aquifers, the phase difference should theoretically be zero, given the absence of poroelastic deformation. However, uncertainties inherent in GPS and GRACE(FO) phase estimations—resulting from the non-stationary nature of the time series, spatial variability, and differing dataset resolutions—lead to relatively small, non-zero phase differences, even in these areas.

To distinguish GPS stations affected by poroelastic deformation from those unaffected, we established a threshold. Stations with phase differences below this threshold are assumed to be free of poroelastic contamination, while those exceeding it are considered impacted. Our analysis of GPS stations not located above aquifers showed that approximately 79% exhibited phase differences within 60 days. Although we expected phase differences to be zero in these regions, the majority of stations fell within this 60-day range, suggesting that this value reasonably accounts for the uncertainty in phase estimations (Fig. 2 subplot).

Additionally, we analyze the average amplitude of all GPS stations in the study area at different phase differences (Fig. 2) and find that the average amplitude of GPS stations not located over aquifers (Fig. 2 red dotted line) is very similar to the average amplitude of stations with phase differences between 0 and 60 days. This further supports the conclusion that phase differences within this range indicate stations unaffected by poroelastic deformation. Conversely, stations with phase differences between 60 and 120 days showed a decline in amplitude, likely due to destructive interference between the elastic loading and poroelastic signals. Beyond this range, amplitude values increased sharply, with a marked rise—exceedingly twice the mean amplitude—observed when phase differences reached 150 to 180 days. This sharp increase strongly suggests dominant poroelastic deformation.

Based on these observations, we set a 60-day phase difference as the threshold for identifying stations potentially contaminated by poroelastic deformation.

2.4 An analysis of the Impact of poroelastic deformation on GPS and GRACE (FO) phase differences

To investigate how poroelastic deformation affects the phase difference between GPS and GRACE(FO) observations, we conducted a simulation experiment with varying amplitudes and lag times of poroelastic deformation. This experiment considers the amplitude and timing of poroelastic deformation, where the amplitude is determined by the physical properties of the aquifer, such as porosity or skeletal storage coefficient (Gualandi & Liu 2021; Ojha et al. 2018; Smith et al. 2017) and the timing of poroelastic deformation is related to the recharge time of the aquifer (Grismer 2013; Hocking & Kelly 2016; Turkeltaub et al. 2015).

In this experiment, we assume that the vertical displacements observed by GPS consist of two components: elastic loading deformation and poroelastic deformation. We modeled these two deformations using harmonic functions—one for the elastic loading deformation (Eq. 7) and the other for the poroelastic deformation (Eq. 8). By summing these functions, we simulated the surface deformation as it would be observed by GPS (Eq. 6). We then estimated the phase for both the combined deformation signal (representing GPS observations) and the elastic loading deformation.

$$V_{\text{GPS}} = V_{\text{elastic}} + V_{\text{poroelastic}} \tag{6}$$

$$V_{\text{elastic}} = Esin(2\pi t) \tag{7}$$

$$V_{\text{poroelastic}} = P\sin\left(2\pi t + \pi - \varphi_{lag}\right), \tag{8}$$

where E and P represent the amplitude factor of elastic loading deformation and poroelastic deformation, respectively. We assume that elastic and poroelastic deformations are precisely anti-correlated when there is no lag, which is why the factor "π" is added to the poroelastic term in Eq. 8. The term φ_{lag} denotes the lag time of poroelastic deformation relative to elastic loading deformation. A positive φ_{lag} indicates that poroelastic deformation lags the elastic loading deformation, while a negative φ_{lag} indicates that load-induced elastic deformation lags the poroelastic deformation. We simulated both scenarios, and since the results are exact opposites (Figures S3 and S4), we only need to analyze the absolute value of the phase difference when applying our method.

As the amplitude of poroelastic deformation exceeds that of the elastic loading deformation, the phase difference

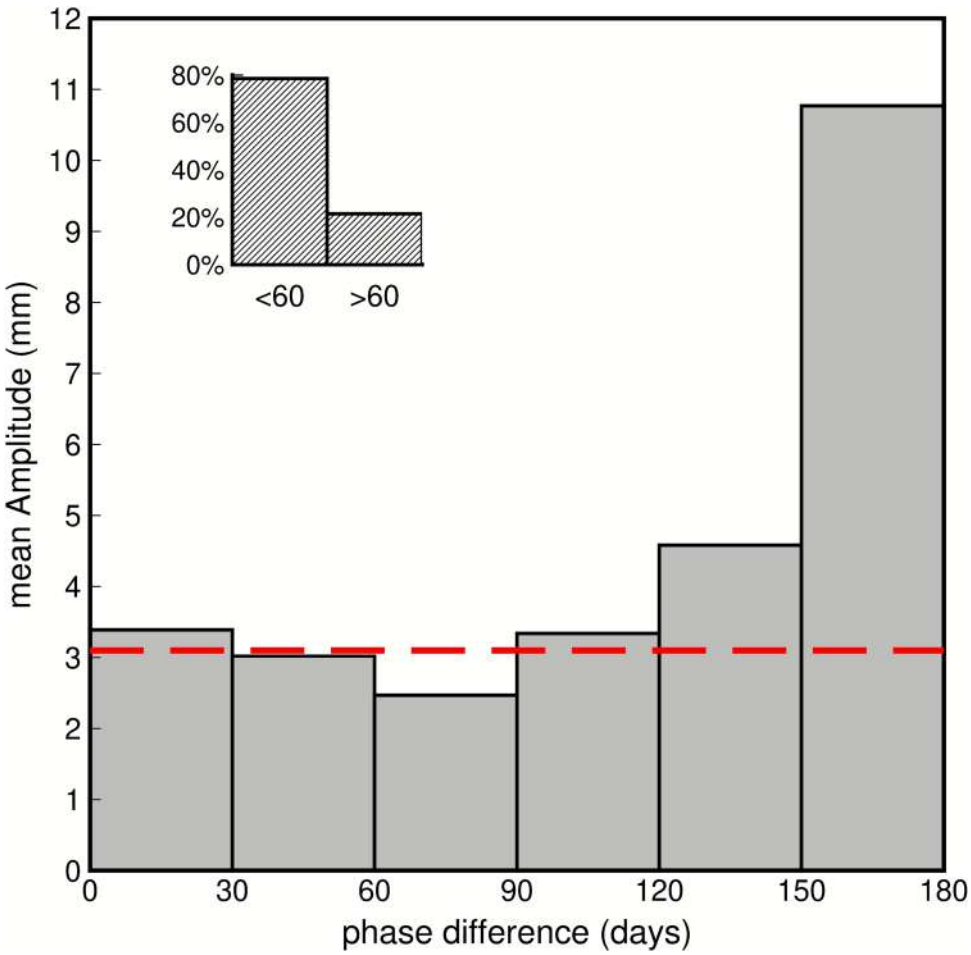

Fig. 2 The gray bars represent the average amplitudes of GPS vertical measurements at 30-day intervals of phase differences. The red dotted line represents the average amplitude of GPS vertical measurements that are not located above known aquifers. The subplot shows the proportion of GPS stations (not located above known aquifers) that fall within different bins of phase differences

decreases progressively with increasing lag time. Additionally, when the lag time remains constant, the phase difference between GPS and GRACE(FO) increases as the ratio of poroelastic deformation to elastic deformation becomes more significant (i.e., as poroelastic deformation dominates the observed surface deformation) (Fig. 3).

The results presented in Fig. 3 illustrate the relationship between the amplitude ratio (P/E) of poroelastic to elastic loading deformation and their respective lag times on the phase difference observed between GPS and GRACE(FO). Figure 3a, b, c demonstrates how varying amplitude ratios of poroelastic to elastic loading deformation impact the phase difference when the lag time is constant. For amplitude ratios of 2, 1, and 0.5, the phase difference becomes smaller as the ratio decreases, as shown by the vertical blue dashed lines in Fig. 3g. Figure 3d, e, f shows the influence of different lag times (0, 30, and 60 days) on the phase difference when the amplitude ratio is held constant, as indicated by the horizontal blue dashed lines in Fig. 3g. These panels suggest that increasing the lag time leads to progressively larger phase differences, highlighting the impact of poroelastic lag on GPS observations. Figure 3g provides a comprehensive overview, where the x-axis represents the lag time of poroelastic deformation relative to elastic loading deformation, and the y-axis represents the amplitude ratio of poroelastic to elastic loading deformation. The color gradient reflects the magnitude of the phase difference between GPS and GRACE(FO), with warmer colors indicating larger phase differences. This panel highlights the direct correlation between higher amplitude ratios and increasing lag times, which jointly contribute to greater phase differences.

The results demonstrate that both the lag time and the relative amplitude of poroelastic deformation compared to elastic loading deformation are critical factors in determining the phase difference between GPS and GRACE(FO) data.

3 Results

3.1 Impact of spatial resolution on phase estimates of load-induced crustal elastic deformation

The spatial resolution of GRACE(FO) data is approximately 300 to 500 km, whereas GPS stations provide point-wise

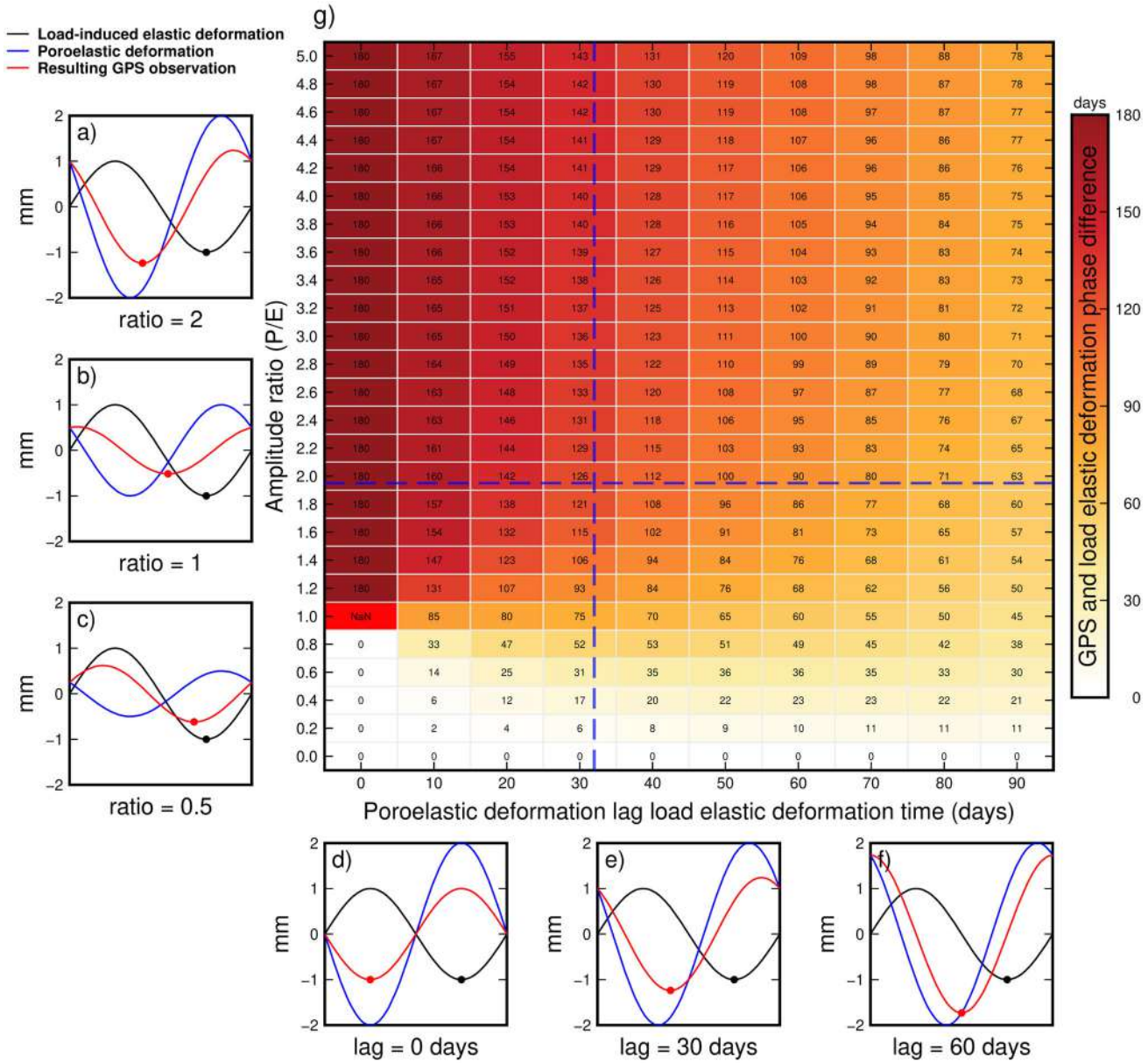

Fig. 3 The effect of different amplitude ratios of poroelastic deformation relative to elastic loading deformation and lag times on the phase difference between GPS observation and elastic loading deformation. Panels **a**–**c** depict the influence of varying amplitude ratios of poroelastic to elastic loading deformation on the phase difference when the lag time is constant, as represented by the vertical blue dashed lines in panel **g**. Specifically, panels **a**, **b**, and **c** correspond to amplitude ratios of 2, 1, and 0.5, respectively. Panels **d**–**f** show the impact of different lag times on the phase difference when the amplitude ratio is constant, as indicated by the horizontal blue dashed lines in panel **g**. These panels represent lag times of 0, 30, and 60 days, respectively. The red and black dots indicate the lowest point within each cycle, and the horizontal distance between them indicates the phase difference between the GPS observations and the elastic loading deformation. Panel **g** provides a comprehensive view of the phase difference under various conditions. The x-axis represents the lag time of the maximum poroelastic deformation relative to the maximum elastic loading deformation, while the y-axis represents the amplitude ratio of poroelastic deformation to elastic loading deformation. The color and value indicate the phase difference between the GPS observations and the elastic loading deformation

measurements with much finer spacing. To ensure that phase estimates derived from such coarse GRACE(FO) data are still representative when compared with higher-resolution data, we first need to assess whether the spatial resolution significantly affects the phase estimates of elastic loading deformation.

We performed a simulation study using monthly TWS estimates from the RTWS5 which captures most local effects, allowing us to assess the impact of resolution on phase estimates. We downsampled the original 0.05-degree grid to coarser resolutions of 0.25, 0.5, 1, 3, and 3-degree, then calculated the phase and amplitude of elastic loading deformation using the same method applied to GRACE(FO) data (Figure S7). We also used the WGHM for assessment (Figure S8).

The results show that the phase of the elastic loading deformation remains largely unaffected by changes in spatial resolution. Although the phase patterns become smoother with coarser resolutions, the variations stay within approximately 30 days (Fig. 4b and 4c, S7 and S8). However, the amplitude variation is significant, with differences of up to twofold as the resolution changes (Fig. 4e, f).

Therefore, we conclude that the spatial resolution of GRACE(FO) has a minimal effect on the phase estimates of elastic loading deformation. This variation is smaller than the uncertainty in the phase difference, which is approximately 60 days (see Sect. 2.3). Consequently, spatial resolution discrepancies between GRACE(FO) and GPS are not the primary cause of large phase differences.

3.2 Comparison of GPS observations and elastic loading deformation

For comparison with existing studies and for validation, we focus on a well-studied region with a dense GPS network. This area, located in the western U.S. (33°N–42°N, 114°W–125°W), covers the Central Valley aquifer system. The Central Valley is critical for supporting California's agriculture, which relies heavily on groundwater. The aquifer system comprises interlayered sand, gravel, silt, and clay, deposited as alluvium. Shallow portions of the aquifer are unconfined, allowing recharge from surface water. However, with increasing depth, finer materials like silt and clay restrict vertical water movement, creating semi-confined or confined conditions (Jagucki et al. 2009). This region has experienced significant stress due to excessive groundwater pumping and prolonged droughts, leading to groundwater depletion and land subsidence, particularly in the Tulare and San Joaquin Basins (Ojha et al. 2018).

NGL provides surface deformation time series data for a total of 1,537 GPS stations in the region. After applying the preprocessing steps detailed in Sect. 2.1, 1,393 stations remained for analysis (Fig. 5a). Several examples of the fitting results using Eq. 1 are shown in Fig. 5b.

In the following, we present the phase estimates based on both GPS and GRACE(FO) data. Figure 6 shows the annual phase and associated uncertainties for vertical displacements observed by GPS and elastic loading deformation estimated by GRACE(FO).

The GPS phase values (Fig. 6a) exhibit greater complexity compared to those from GRACE(FO) (Fig. 6c), which is expected for point-wise measurements. In the northern part of the study region, GPS phases are approximately 270 days. However, along the coastal areas (south of 38°N), within the Central Valley, and in urban centers like Los Angeles, GPS phases show a wide range of variation. Many GPS stations in the Central Valley and Los Angeles display a distinct poroelastic response linked to significant groundwater depletion (Ojha et al. 2018; Riel et al. 2018; Scanlon et al. 2012; Smith et al. 2017). These stations typically exhibit a six-month phase difference compared to nearby GPS sites. In contrast, the phase estimates from GRACE(FO) (Fig. 6c) are more consistent across the study area. Figures 6b and 6d illustrate the phase uncertainties for both GPS and GRACE(FO) data, respectively. After filtering out stations with phase uncertainties greater than 15 days, 62 stations (4% of the total) were removed due to significant observational errors and discontinuities. The remaining stations exhibit lower uncertainties, ensuring that our method can be reliably applied in further analyses.

Figure 7 highlights the phase differences between GPS-observed annual vertical displacements and GRACE(FO) estimated elastic loading deformation at each GPS station. Most phase differences range between 0 and 60 days (Fig. 7a), with 84% of the stations showing predominantly elastic loading deformation. The remaining 16% of stations, identified as being dominated by poroelastic deformation using the proposed method are mainly located within the Central Valley and other well-known aquifer systems (https://www.usgs.gov/national-hydrography/watershed-boundary-dataset, accessed on September 15, 2023) (Fig. 7b).

3.3 Positioning within previous literature

As noted in the introduction, there is currently no consensus on a method to identify GPS stations affected by poroelastic deformation. Most previous studies rely on empirical identification methods proposed by Argus et al. (2017) and Carlson et al. (2022). For example, Argus et al. (2017) define a site as being influenced by poroelastic deformation if its seasonal amplitude exceeds 3 mm and its peak occurs around April, or if its surface subsidence rate is greater than 2.5 mm/year. Similarly, Carlson et al. (2022) set a threshold of 2 mm for seasonal amplitude, with a peak between March 1 and May 31, or a subsidence rate over 2.5 mm/year. Given the similarity of these approaches, with only slight differences in

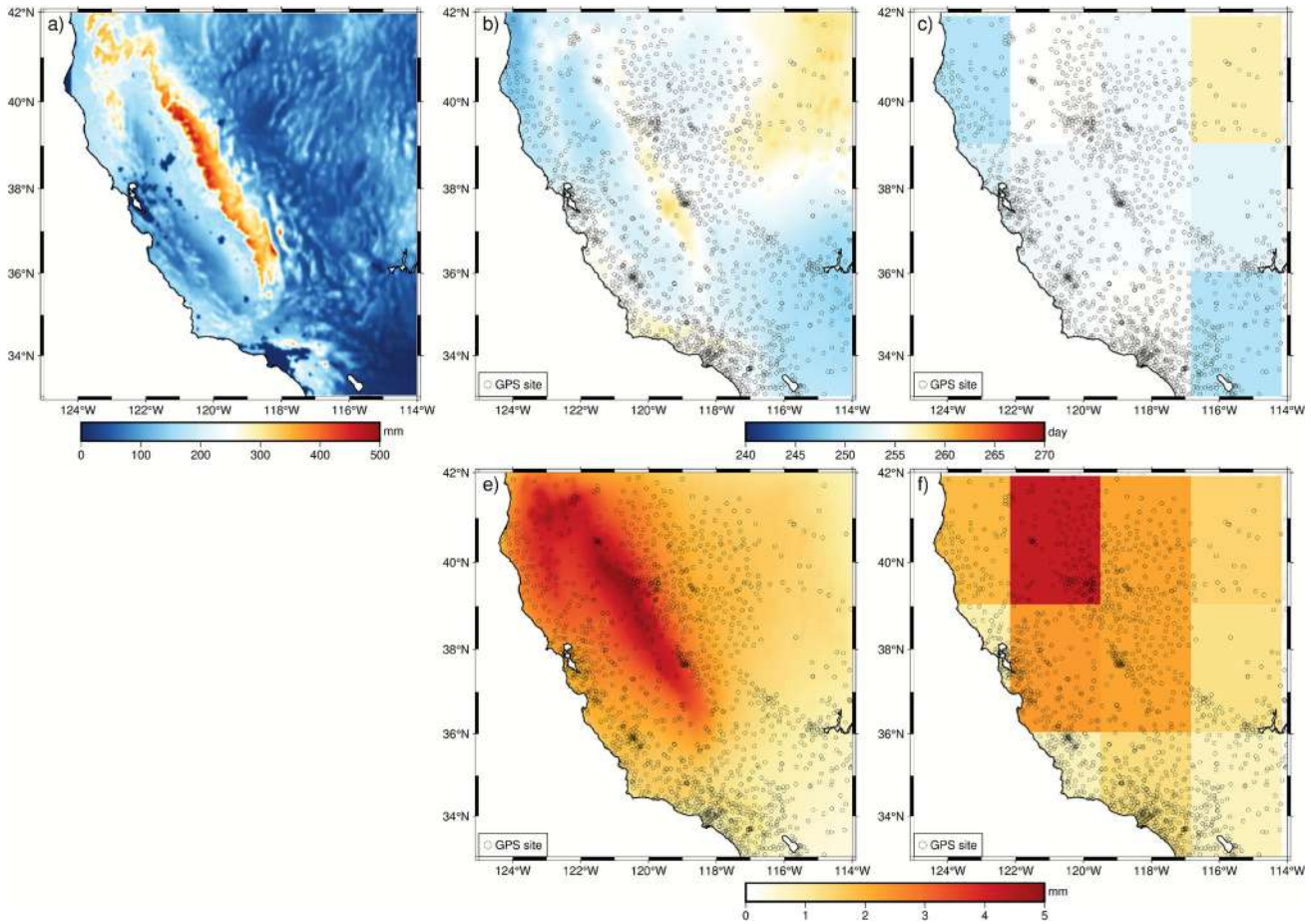

Fig. 4 Panel (a) shows the spatial distribution of TWS in January 2002 for the RTWS5 product. Panels (b) and (e) show phases and amplitude of annual, vertical-component elastic loading deformation calculated based on the RTWS5 product at 0.05. And panels (c) and (f) show phases and amplitude at 3-degree resolutions

thresholds, we only replicated Carlson et al.'s (2022) method to compare with our results. As shown in Fig. 8a, Carlson et al. (2022) identified 162 stations, while our phase-based method identified 201 stations (Fig. 8c). As we will demonstrate later in Sect. 4.2, the unidentified stations lead to anomalies in specific locations.

In addition to the traditional approach, we also reproduced the correlation-based method recently proposed by Carlson et al. (2024). This method quantifies the correlation coefficient between GPS-observed vertical displacement and the elastic loading deformation inferred from GRACE(FO) data. Stations with correlation coefficients below 0.3 are flagged as being influenced by non-elastic loading signals, including poroelastic deformation. As shown in Fig. 8b, the correlation-based method identified 214 stations, capturing more poroelastically influenced stations than the trend and amplitude method and phase-based method.

We found that 72 GPS stations were identified by both the correlation-based and phase-based methods. Our approach successfully identified all stations flagged by Carlson et al. (2022)'s method based on amplitude threshold. However, some stations identified by Carlson et al. (2022)'s trend-based threshold were not detected by our method. These comparisons provide a quantitative basis for evaluating the differences among the three approaches. Discussions related to these differences can be found in Sect. 5.

4 Validation

4.1 Verification of GPS sites affected by poroelastic deformation

To validate our identification of GPS sites affected by poroelastic deformation (Fig. 7c), we first isolated the poroelastic component from the GPS-observed vertical displacements and compared it with the elastic loading deformation calculated from GRACE(FO) data. The poroelastic deformation was isolated using the following equation:

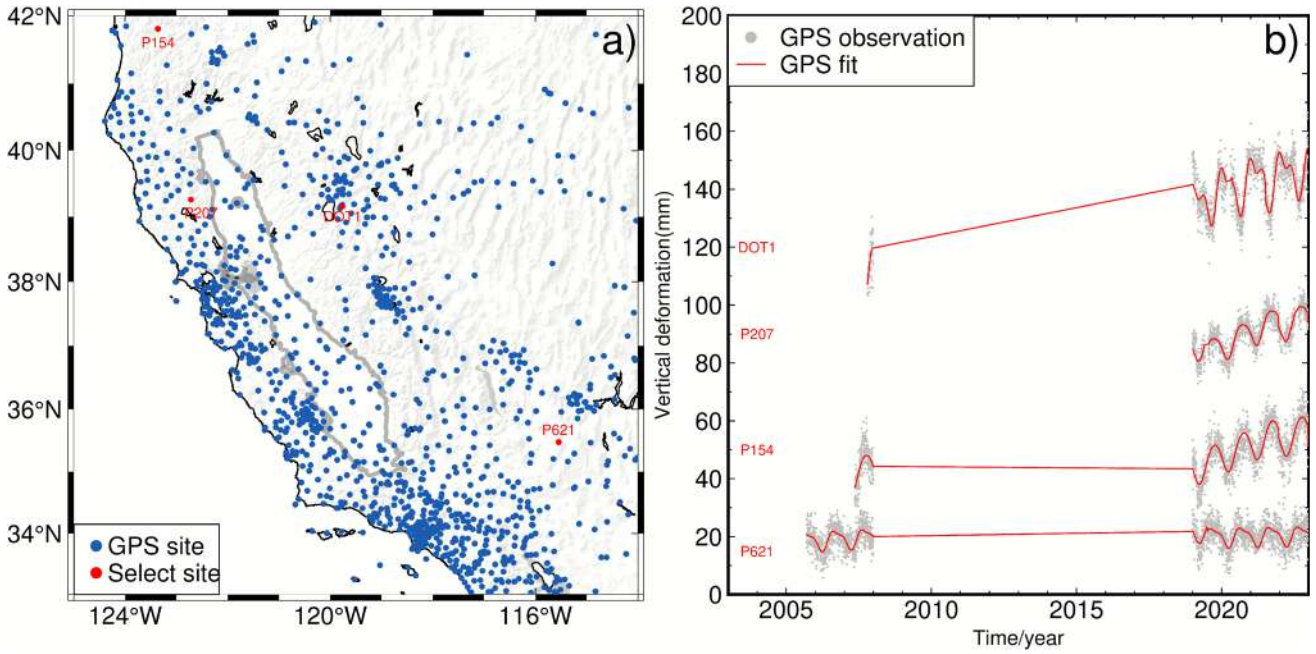

Fig. 5 **a** Map of the study area, with GPS stations shown in blue. The gray polygon indicates the Central Valley boundary. **b** Vertical displacement time series (gray dots) and model results (red lines) for four randomly selected stations. The offsets in the GPS time series, primarily due to equipment changes or abrupt shifts, are provided by NGL

$$V_{poroelastic} = V_{GPS} - V_{elastic} - V_{NTAL} - V_{NTOL} - V_{GIA}, \quad (9)$$

where V_{NTAL} and V_{NTOL} represent vertical displacements due to non-tidal atmospheric and oceanic loading, which were removed earlier in the analysis. To ensure consistency between the GPS and GRACE(FO) datasets, we also removed the GIA effect using the ICE6G-D model (Peltier et al., 2018), although this step was not required for phase calculations. The elastic loading deformation $V_{elastic}$ was computed from GRACE(FO) data (Eq. 2). As we have demonstrated in Fig. 4, the amplitude estimates derived from the coarse GRACE(FO) product are not representative at finer resolution, for most cases, the amplitude derived from a coarse resolution of 3-degree grid is about two times smaller than that on a 0.05-degree grid. Therefore, we do not expect that this procedure can completely clean the elastic loading deformation.

We neglected contributions from other geophysical processes, such as tectonic activity, sediment compaction and volcanism, as well as other sources of time series error. Next, we calculated the phase differences between the estimated poroelastic deformation (Eq. 9) and the elastic loading deformation from GRACE(FO). Nearly all stations displayed a phase difference of approximately 180 days (Fig. 9a), consistent with the theoretical expectation that these two processes should be anti-correlated. It is important to note, however, that not all identified stations allowed for the computation of poroelastic deformation. This limitation arises from the requirement that both ITRF2020-based GPS time series and GRACE data must have at least one full year of overlapping observations, which is not always satisfied in the currently available datasets. As a result, the number of stations shown in Fig. 9a is smaller than that in Fig. 8c.

Given the close relationship between poroelastic deformation and groundwater level variations, we compared the isolated poroelastic deformation with groundwater level observations from nearby wells (Fig. 9b). Specifically, we analyzed the annual phases of poroelastic deformation alongside groundwater level fluctuations. Since groundwater level changes can vary significantly between wells located just tens of kilometers apart, we limited our comparison to wells within 10 km of GPS stations and with low phase uncertainty (uncertainty of the phase < 30 days).

The results show that, for most wells, the phase of groundwater level changes aligns closely with the poroelastic deformation estimated from GPS displacements, further supporting the accuracy of our identification method. After removing the elastic loading deformation from GPS observations, we expect the remaining poroelastic deformation to more closely align with well measurements, and this is indeed observed at most sites. However, in some cases, GPS stations exhibit a notable phase difference with nearby wells. This discrepancy may arise from inherent difference in amplitude

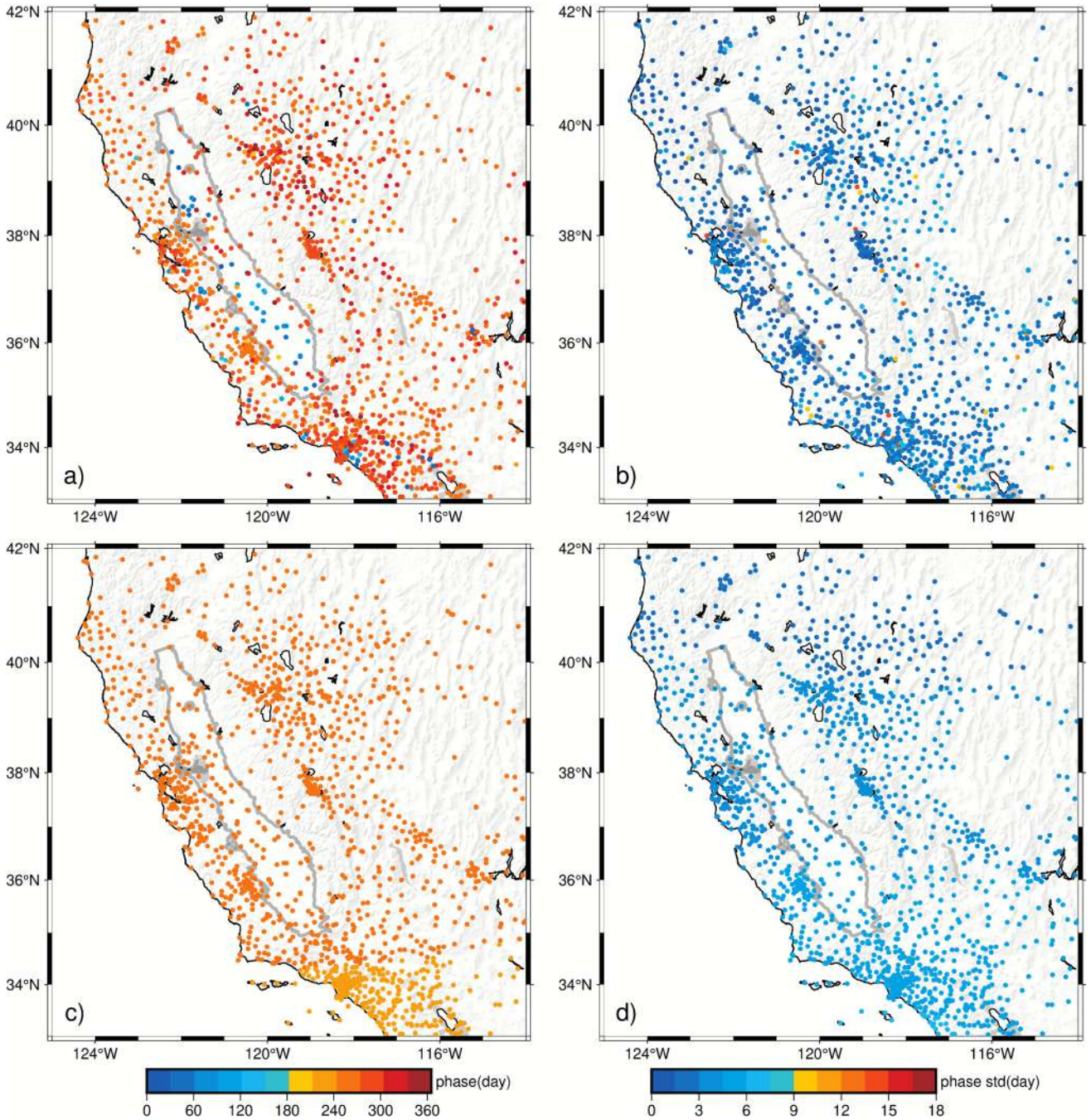

Fig. 6 **a** Annual phase estimates of the vertical component from GPS observations. **b** Standard deviations of phase estimates for GPS observations. **c** Annual phase estimates of the estimated load-induced crustal elastic deformation from GRACE(FO). **d** Standard deviations of phase estimates for GRACE(FO) load-induced crustal elastic deformation. The gray polygon outlines the Central Valley boundary

between GPS and GRACE(FO), which could lead to erroneous estimations of the poroelastic component.

4.2 Implications for GPS estimates of TWS

The large number of GPS stations in the study area allows us to invert mass changes at a relatively high spatial resolution (approximately 25 km). We subdivide the study area into a 0.25×0.25-degree grid. Using the vertical displacements of

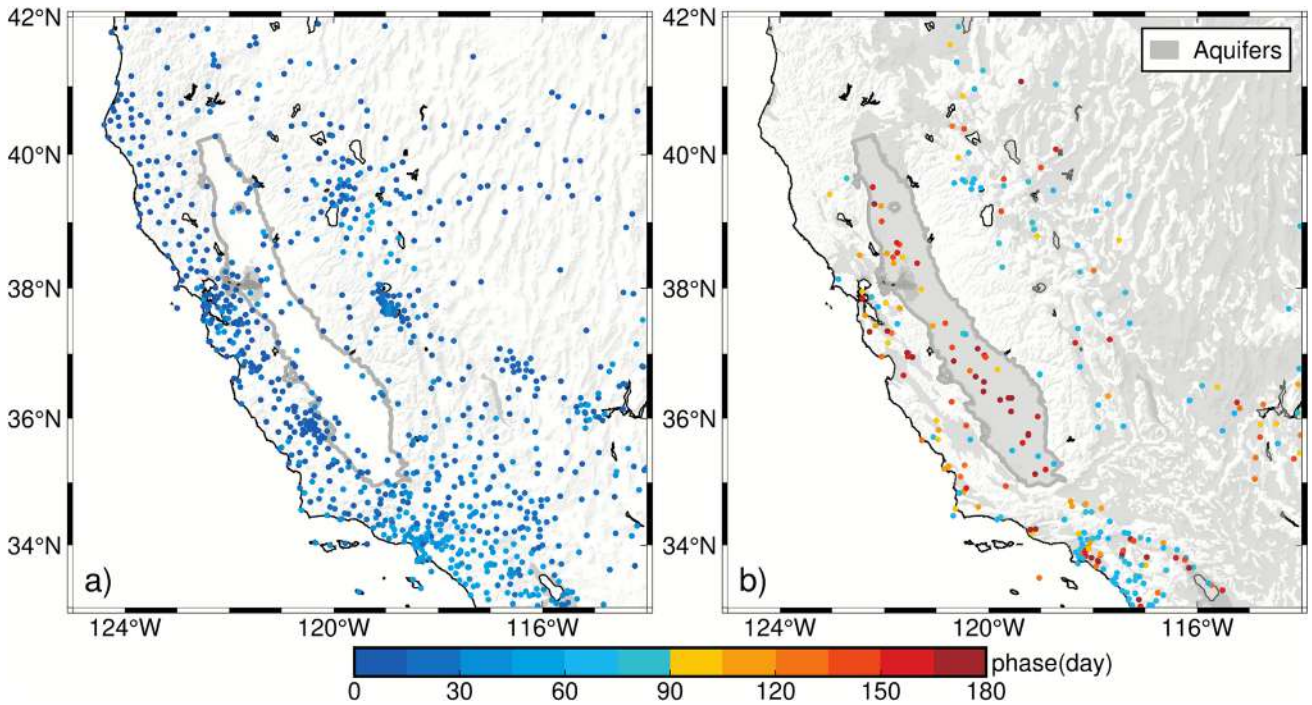

Fig. 7 Annual phase differences between GPS-observed vertical displacements and load-induced elastic deformation from GRACE(FO). **a** GPS stations with phase differences between 0 and 60 days. **b** GPS stations with phase differences greater than 60 days. Gray-shaded areas indicate known aquifer systems

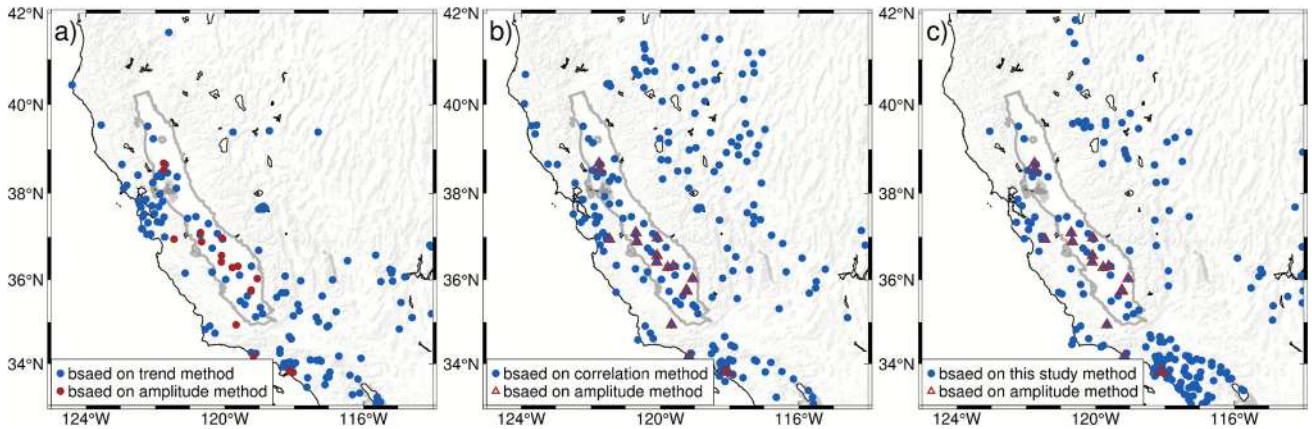

Fig. 8 GPS sites contaminated by poroelastic deformation identified by different methods. Panel a shows the identification results using trend and amplitude-based method. Panel b shows the identification results of the correlation method in this study. Panel c shows the identification results of the phase difference method in this study

GPS stations as constraints, we can follow a Green's-function approach to solve for changes in TWS across the study region (Argus et al. 2014; Farrell 1972; White et al. 2022; Zhong et al. 2020). For point loads, a load-induced vertical elastic displacement can be expressed as follows:

$$v = GM + \varepsilon_{error}\,, \tag{10}$$

where v represents the vertical displacement (in meters), M is the mass of the load (in kilograms), ε_{error} is the observe error, and G stands for the loading Green's matrix based on preliminary reference earth model (PREM) (Dziewonski & Anderson, 1981) at an angular distance between the point load and the GPS station. To solve for the mass change, we minimize the following:

$$min\{\|GM - v\|^2\} \tag{11}$$

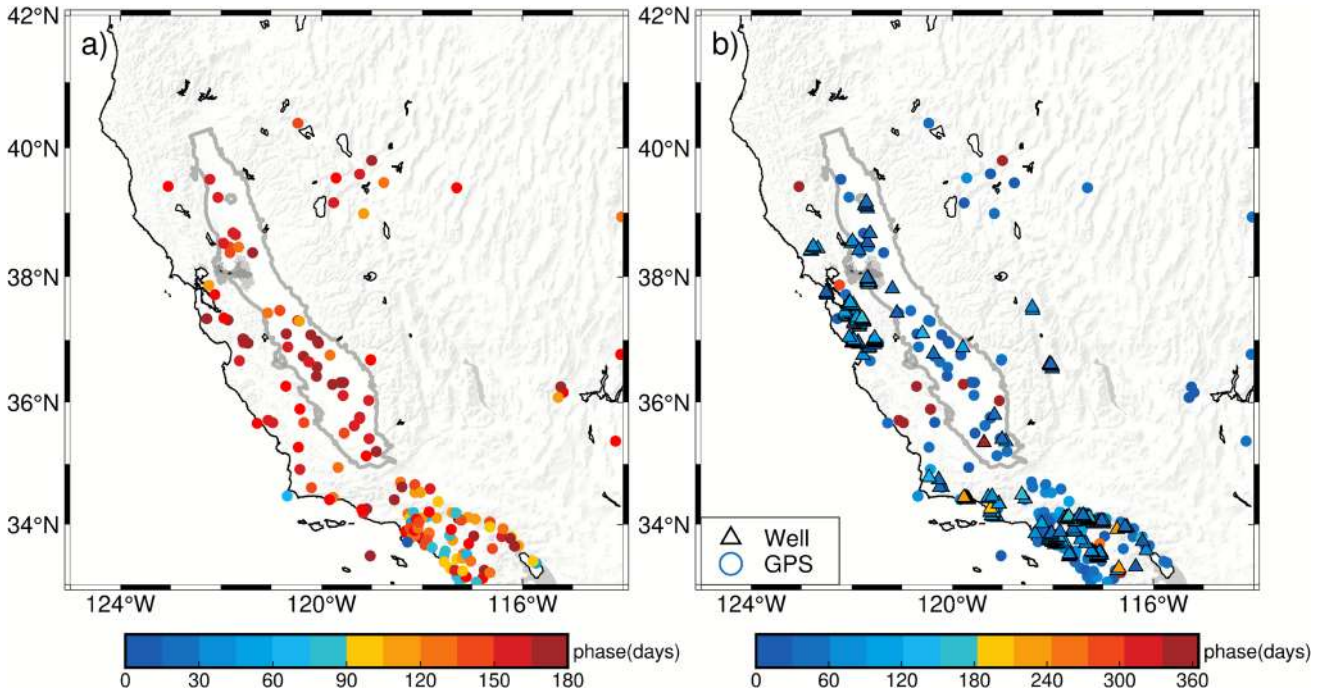

Fig. 9 Phase comparison between poroelastic deformation, elastic loading, and groundwater level variations. **a** Annual phase differences between poroelastic deformation and load-induced crustal elastic deformation. **b** Comparison of phases between poroelastic deformation estimated from GPS stations and groundwater level changes at nearby wells

Since the number of unknown parameters of mass change is much larger than the GPS observations, additional constraints are needed. The desired result is a grid of mass changes across the region, the smoothness between neighboring pixels must be considered in the calculation process. Here, the Laplace operator L is used as an additional constraint to favor spatially smooth solutions. The equation is as follows:

$$M = \left(G^T G + kL^T L\right)^{-1} G^T v\,, \tag{12}$$

where k is a roughness factor that is applied to the smoothing constraint. Here, we chose the Generalized Cross-Validation (GCV) method to determine the roughness factor. This method determines the best coefficient 0.014 by solving for the variable corresponding to the GCV function when it obtains the minimum residuals (Golub et al. 1979). Please note that this value was obtained based on the inversion results after excluding poroelastically contaminated stations identified by the trend-to-amplitude method. To ensure consistency and comparability across different identification strategies, this same coefficient was applied to all subsequent inversions, regardless of the station selection method.

We calculated TWS changes relative to the mean storage over the study period, based on GPS data from April to October 2022 (using Eq. 12). Figures 10a and d show the results using all GPS sites for inversion. The result without removing the contaminated stations is clearly problematic because an unexpected increases of TWS appears in the Central Valley. In California, however, snow and water at Earth's surface attain a maximum in April (at the end of the winter) and a minimum in October (at the end of the summer), making this increase physically implausible.

To address this, we tested three station exclusion strategies. Figure 10b, e presents results after removing stations primarily affected by poroelastic deformation, following trend and amplitude-based method. While this improves the accuracy in the southern Central Valley by reducing erroneous signals, the northern Central Valley still presents problematic signals when compared to the GRACE(FO) results (Fig. 10h, k). Although the GRACE(FO) resolution limits direct validation, the observed pattern is inconsistent with any known hydrological behavior and physical processes. Figure 10c, f shows results after applying correlation method to exclude poroelastically affected stations and Fig. 10g, j shows results after applying our phase method. In both cases, the erroneous signals in the Central Valley are entirely removed, yielding more physically consistent patterns.

The residual maps and their corresponding histograms (Fig. 11) provide further insights into the inversion quality. These residuals represent the difference between the original

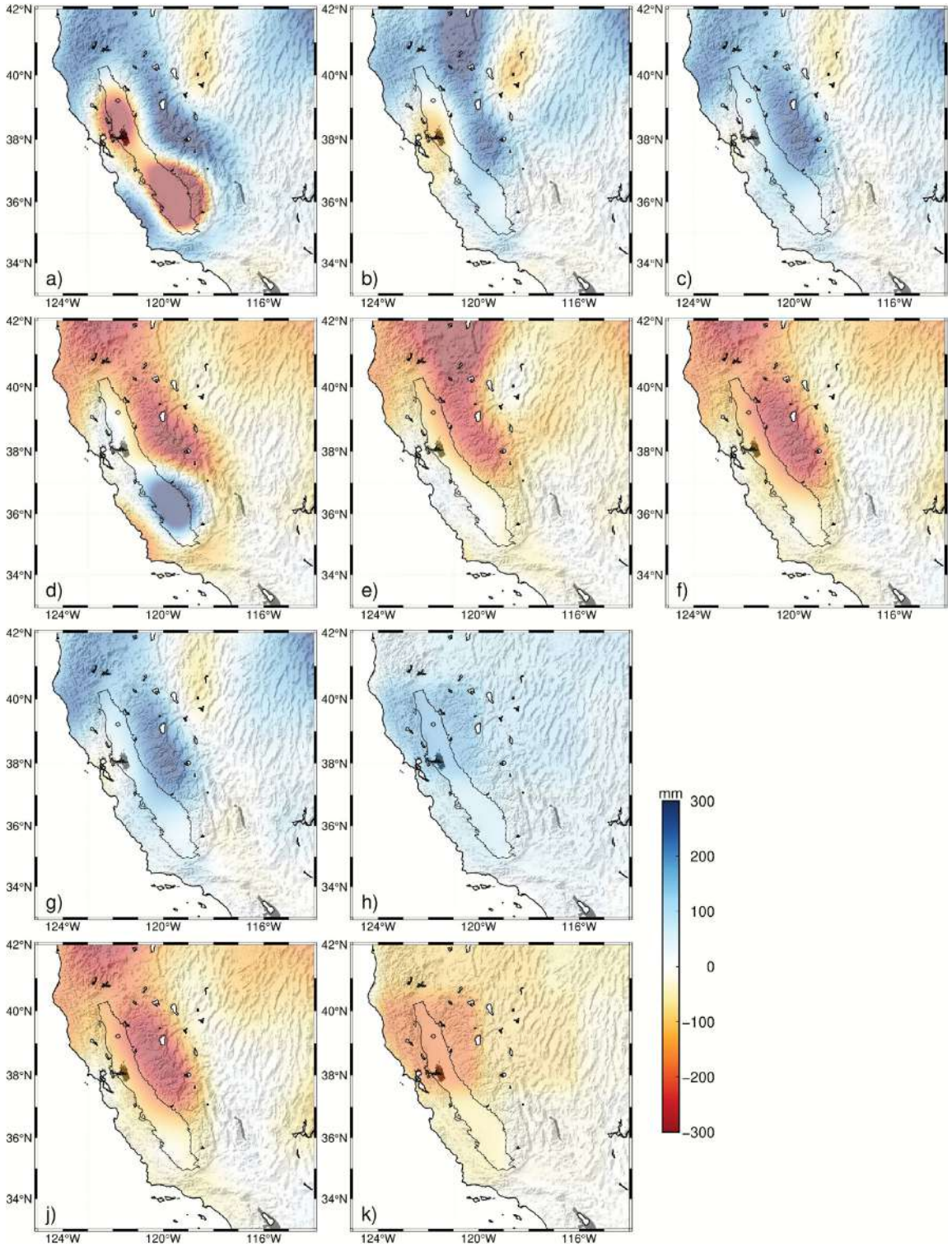

Fig. 10 California TWS estimated using GPS and GRACE(FO) data. Panels **a**–**c**, **g**, and **h** show TWS in April 2022, while panels **d**–**f**, **j**, and **k** show TWS in October 2022. Panel **a** and **d** includes all GPS stations in the inversion. Panels **b** and **e** exclude 162 GPS stations affected by poroelastic deformation identified by trend and amplitude method in Fig. 8a. Panels **c** and **f** exclude 214 GPS stations affected by poroelastic deformation identified by correlation-based method in Fig. 8b. Panels **g** and **j** exclude 201 GPS stations affected by poroelastic deformation identified by our phase-based method in Fig. 8c. Panels **h** and **k** show the TWS inferred from GRACE(FO)

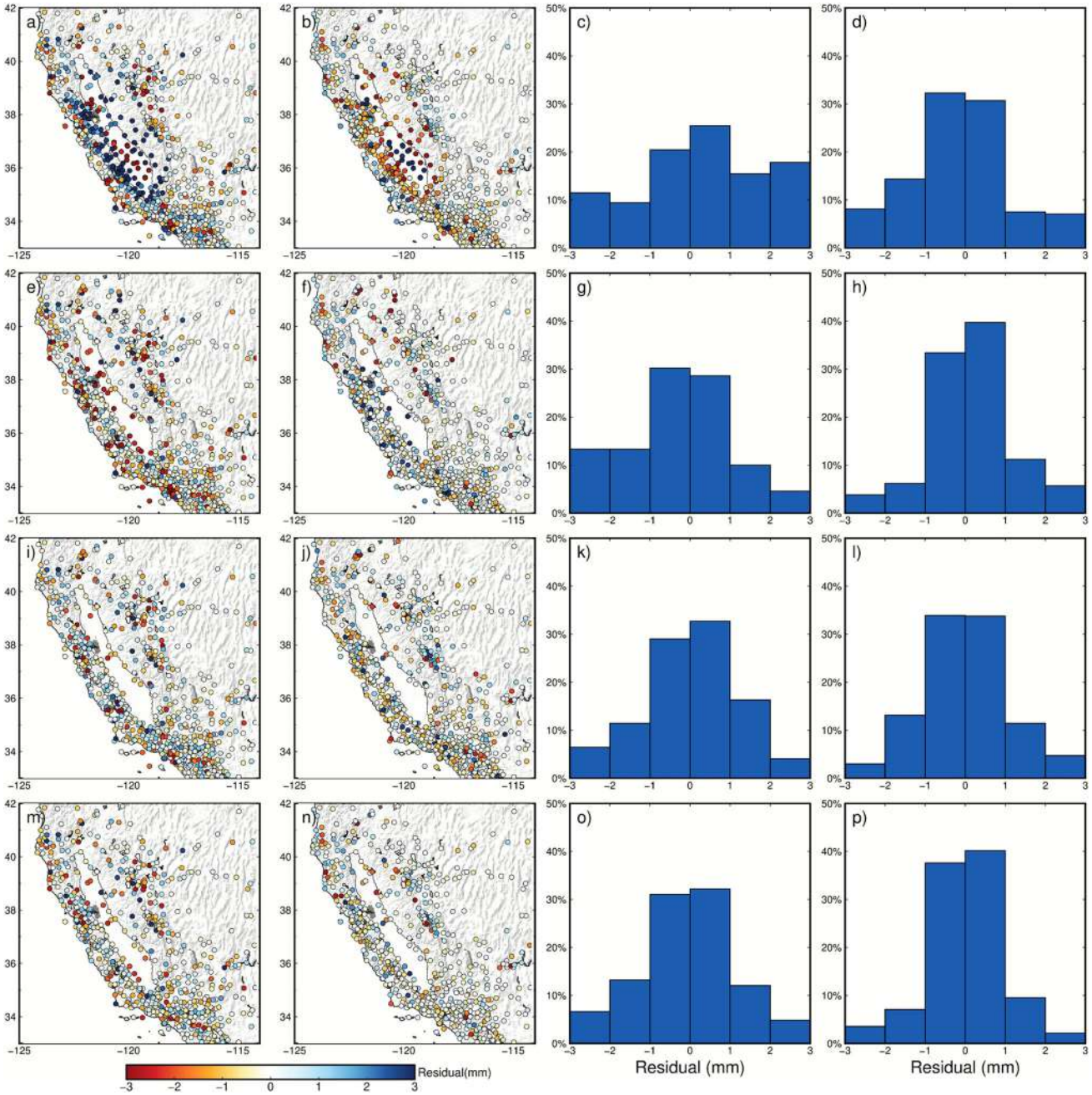

Fig. 11 Inversion residuals and histograms under different station exclusion strategies. Panels **a** and **b** show GPS residual when using all GPS stations, with corresponding histograms in panels **c** and **d**. Panels **e** and **f** present residual results after excluding stations identified by the trend and amplitude method, with corresponding histograms in panels **g** and **h**. Panels **i** and **j** show residuals after excluding stations based on the correlation method, with corresponding histograms in panels **k** and **l**. Panels **m** and **n** display residuals after excluding stations identified by the phase method, with corresponding histograms in panels (o) and (p)

GPS vertical displacements and those re-predicted by forward modeling the inferred surface mass load using Green's functions. Therefore, they directly reflect the internal consistency of the inversion–forward modeling loop. When using all GPS stations (Fig. 11a, d), the residuals are large, spatially uneven, and the histogram is wide and asymmetric (Fig. 11c, d), with many values exceeding ± 2 mm. This suggests significant misfits and low model consistency. After removing poroelastic-contaminated stations based on trend and amplitude method (Fig. 11e, f), the residuals become more spatially homogeneous, and the histogram distribution narrows slightly (Fig. 11g, h), indicating some improvement.

In contrast, the correlation-based method (Fig. 11i, j) leads to a clearer reduction in both the magnitude and spatial variability of the residuals. The corresponding histogram shows residuals concentrated around zero (Fig. 11k, l), mostly within ± 2 mm, indicating greater internal consistency of the inversion results. The phase-based method (Fig. 11m, n) yields the most favorable outcome. The residuals are not only minimal and spatially uniform but also exhibit the tightest and most symmetric histogram among all approaches (Fig. 11o, p). The residual distribution is nearly Gaussian, sharply peaked at zero, and largely constrained within ± 1 mm. This reflects the highest degree of consistency between the observed and re-predicted displacements.

Overall, while both the correlation-based and phase-based methods significantly improve inversion reliability compared to using all stations or the trend and amplitude criteria, the phase-based method offers the greatest enhancement. It minimizes modeling errors and suppresses poroelastic contamination more effectively, leading to a more robust and physically consistent inversion of TWS changes.

5 Discussions

The phase-based method provides a robust and physical approach for identifying GPS stations affected by poroelastic deformation, particularly in cases where conventional metrics such as surface subsidence trend or amplitude may be ineffective. By focusing on the annual phase of vertical deformation, an important advantage of our method is that it is tightly linked to hydrological cycles and less influenced by longer-term processes such as tectonic motion, GIA, and sediment compaction.

A key factor underlying the effectiveness of our approach is a fundamental geophysical property: phase estimates of load-induced elastic deformation are not highly sensitive to spatial resolution. Although this may seem counterintuitive, it reflects the rigidity of the crust—significant elastic deformation requires large-scale hydrological loading, so localized differences in loading have minimal impact on the deformation phase. This property, demonstrated in Sect. 3.1, allows us to use phase estimates derived from coarse-resolution GRACE(FO) data and still obtain meaningful comparisons with higher-resolution observations.

The comparisons in Sect. 3.3 highlight that the three identification approaches differ in both the number and spatial distribution of stations flagged as affected by poroelastic deformation. The phase-based method identifies more GPS stations affected by poroelastic deformation compared to trend and amplitude-based method. This increase is expected, as trend and amplitude-based methods are inherently limited to detecting stations where poroelastic deformation is much larger than elastic loading deformation and where the two signals occur simultaneously. In such cases, GPS observations exhibit anomalously large amplitudes and phase estimates that cluster within a few months. However, as demonstrated in Fig. 3, stations with smaller amplitudes or seasonality outside the predefined peak window can still be influenced by poroelastic deformation. A simple relaxation of the threshold may be ineffective for identifying additional stations, as the criteria do not simultaneously account for both amplitude ratio and lag time. In addition, some stations identified by Carlson et al. (2022)'s trend-based threshold were not detected by phase-based method. These stations with large trends are not necessarily experiencing compaction of aquitards due to groundwater depletion; instead, they may reflect localized sediment compaction, tectonic movement, slow-moving landslides, or other non-hydrological signals. Uncertainties in the GIA model can also affect estimated trends, and offsets or discontinuities in the GPS time series may further bias trend estimates. These factors contribute to the discrepancies between the two identification approaches.

More importantly, previous studies have shown that groundwater depletion does not always lead to surface subsidence; in some cases, it may cause surface uplift (Overacker et al. 2022). For example, in the southern High Plains Aquifer, Overacker et al. (2022) found crustal uplift of up to 2 mm/year due to groundwater loss. In such instances, identification methods based on subsidence rates or correlation are ineffective. However, using our method, these stations can be accurately identified (Figure S9). The High Plains Aquifer study also indicates that surface subsidence or uplift depends largely on the magnitude of elastic loading deformation relative to poroelastic deformation.

Carlson et al. (2024) proposed using the correlation coefficient between GPS observations and GRACE(FO)-inferred elastic loading deformation. This method is similar to ours, as larger phase differences correspond to lower correlation coefficients. Interestingly, in the absence of trend signals, Carlson et al.'s correlation coefficient threshold of 0.3 corresponds to a phase difference of approximately 60 days, matching our chosen 60-day threshold. However, correlation analysis can be strongly influenced by long-term trends, especially in cases where groundwater loss causes surface uplift rather than subsidence, the seasonal phase can be opposite to elastic deformation, yet the long-term trend similarity may still yield a high correlation coefficient, potentially masking poroelastic effects. It is also sensitive to non-hydrological trends (e.g., tectonics, GIA), record length, and missing data. These factors can influence correlation values, causing the correlation-based approach to flag a larger number of stations as "affected," even when the deformation is not primarily poroelastic. This explains why the correlation-based method identifies the most stations among all methods tested. In contrast, phase-based method isolates the seasonal component through harmonic fitting, making it more robust to these

confounding factors. Moreover, it provides physically interpretable insights, for instance, by determining the magnitude of both deformation types, we can analyze the lag between the two signals, as shown in Fig. 3. This information helps infer important aquifer properties, such as porosity and skeletal storage coefficients (Carlson et al. 2020; Ojha et al. 2018; Valley 2009), as well as the depth of the vadose zone and groundwater recharge times, key insights for understanding groundwater changes, surface deformation mechanisms, and aquifer dynamics (Crosbie et al. 2013; de Vries & Simmers 2002; Gurdak & Roe 2010; Yang et al. 2019). While phase-based method is helpful for identifying poroelastic responses, a combined analysis using phase, trend, and correlation would be more suitable for broader load-modeling applications, where all non-loading processes should be considered and excluded.

Moreover, we note that Carlson et al. (2024) retained only 490 stations after excluding sites with low correlation. In contrast, our analysis included significantly more stations. This difference is partly due to the sensitivity of correlation analysis to the length of the GPS time series. Specifically, Carlson et al. (2024) used data based on the IGS14 solution, which provides longer time series for many stations. Our study, however, utilized the more recent IGS20 solution, which despite offering improved precision, covers a shorter temporal span, as it includes data from fewer years. This shorter data record may limit the effectiveness of correlation-based methods, whereas our phase-based approach remains applicable under such constraints.

Our results also suggest that not all GPS stations within aquifer systems are affected by poroelastic deformation. This is likely because unconfined aquifers, which allow upward movement of the water table and coupling with the atmosphere, form a constant pressure boundary that prevents significant poroelastic deformation. In contrast, confined aquifers are isolated from external pressures, so changes in water levels can cause significant pressure variations, leading to poroelastic deformation (Vasco et al. 2022).

Interestingly, not all identified GPS stations contaminated by poroelastic deformation are located directly over major aquifer systems. This could indicate the presence of minor, unmapped aquifer systems or be due to GPS sensitivity to local effects such as snow, lakes, reservoirs, and soil moisture. These localized effects can significantly alter seasonal variations, causing the GPS phase to deviate from the reference phase, which remains unaffected by local processes. Additionally, vertical land motion recorded by GPS may be influenced by factors beyond load-induced elastic and poroelastic deformation, such as thermal expansion of bedrock (Xu et al. 2017) and draconitic errors in GPS data (Rodriguez-Solano et al. 2014). While our method addresses these factors with a 60-day phase threshold, future advancements in geodetic techniques will provide more detailed insights into localized processes, offering a clearer understanding of regional climate dynamics.

While our phase-based method effectively identifies poroelastic deformation driven by seasonal groundwater fluctuations, it may be less effective in deep confined aquifers where groundwater recharge is limited, and seasonal signals are weak or absent. In such settings, characterized by low hydraulic conductivity and slow vertical flow, poroelastic deformation may be dominated by long-term trends rather than seasonal cycles (Shirzaei et al. 2019). In these cases, annual phase differences may fail to capture the poroelastic response. Incorporating long-term vertical deformation trends into the analysis may improve the identification of affected stations. However, this approach requires a detailed understanding of regional long-term variations in both TWS and GWS. Specifically, only when the long-term trend in surface deformation aligns with that of groundwater storage and opposes the trend in load-induced elastic deformation by total terrestrial water storage changes can we reasonably attribute the deformation to poroelastic effects. Without such constraints, trend-based assessments may lead to misclassification.

6 Conclusions

This study presents a phase-based method for identifying GPS stations affected by poroelastic deformation, based on the annual phase difference between GPS-observed vertical displacements and GRACE(FO)-inferred elastic loading deformation. Stations with phase differences exceeding 60 days are classified as contaminated by poroelastic effects. This method leverages the distinct phase behavior of elastic and poroelastic deformation and provides a simple, physically grounded criterion for station screening.

The results confirm that stations dominated by poroelastic deformation are in phase with groundwater-well data and out of phase with elastic deformation, supporting the theoretical assumption that these processes are anti-correlated. Also, the inverted TWS results based on GPS data, after excluding contaminated stations using our proposed method, are more accurate and realistic than those obtained from previously used methods. Thus, we conclude that our method provides a more effective approach for identifying problematic GPS stations.

While removing contaminated stations improves inversion accuracy, it reduces spatial coverage, especially in critical regions such as the Central Valley. To address this, Carlson et al. (2024) proposed a more integrated solution by jointly modeling elastic and poroelastic deformation within the TWS inversion framework. While this approach offers theoretical advantages and improved spatial coverage, it

requires detailed knowledge of aquifer properties, including compressibility, thickness, and Poisson's ratio, which are typically only available in well-studied aquifer systems. In regions with poorly understood or spatially heterogeneous hydrogeology, applying such joint models is often infeasible. In contrast, our method avoids the need for site-specific aquifer parameters and is easier to implement across diverse geographic settings.

Looking ahead, the integration of GPS, GRACE(FO), and InSAR data in joint inversion frameworks remains a promising direction, particularly for retaining GPS stations affected by mixed deformation sources. However, until such models become widely applicable, phase-based method offers an easy and useful tool for identifying GPS stations influenced by poroelastic deformation to improving TWS estimation in groundwater-stressed regions.

Supplementary Information The online version contains supplementary material available at https://doi.org/10.1007/s00190-026-02031-2.

Acknowledgements We would like to express our gratitude to all three anonymous reviewers for their time and insightful comments, which have greatly improved this paper. The authors also wish to thank Hilary Martens for her invaluable contributions, including her constructive suggestions during the early stages of the manuscript and her thorough review of both the initial and revised versions. This study was supported by the National Natural Science Foundation of China (grant 42171426, 42374041 and 42304099) and National Key Research and Development Program of China (2025YFE0102700).

Author Contributions FL and YS conceived the idea and designed all the experiments; FL and YS performed the research and analyzed the data; NT performed RTWS5 simulation; FL, YS, and NT wrote the paper; SZ and BZ reviewed and commented on the paper.

Funding Natural Science Foundation of China, 42171426, Yu Sun, 41801393, Yu Sun, 42304099, Yu Sun, National Key Research and Development Program of China, 2025YFE0102700, Yu Sun

Data availability GPS time series were downloaded from the Nevada Geodetic Laboratory (http://geodesy.unr.edu). The non-tidal atmosphere and ocean loading displacements were downloaded from http://esmdata.gfz-potsdam.de:8080/repository/entry/show?entryid=80daee1b-ff73-481f-b0f3-18026282c03e and http://esmdata.gfz-potsdam.de:8080/repository/entry/show?entryid=94df5183-aec2-41b5-ac14-e785a3e30c15. GRACE JPL mascon data are available at https://grace.jpl.nasa.gov/data/get-data/jpl_global_mascons/, CSR mascon data are available at https://www2.csr.utexas.edu/grace/RL06_mascons.htm, and GSFC mascon data are available at https://earth.gsfc.nasa.gov/geo/data/grace-mascon. WGHM hydrological model data are downloaded from https://doi.pangaea.de/10.1594/PANGAEA.948461. Well data and aquifer data are available at https://waterdata.usgs.gov/. The Regional TWS Simulation at 5 km (RTWS5) product can be obtained from https://www.alice-lab.com.

Declarations

Conflict of interest The authors declare that they have no conflict of interest.

References

Amos CB, Audet P, Hammond WC, Bürgmann R, Johanson IA, Blewitt G (2014) Uplift and seismicity driven by groundwater depletion in central California. Nature 509(7501):483–486. https://doi.org/10.1038/nature13275

Argus DF, Fu Y, Landerer FW (2014) Seasonal variation in total water storage in California inferred from GPS observations of vertical land motion. Geophys Res Lett 41(6):1971–1980. https://doi.org/10.1002/2014GL059570

Argus DF, Landerer FW, Wiese DN, Martens HR, Fu Y, Famiglietti JS, Thomas BF, Farr TG, Moore AW, Watkins MM (2017) Sustained water loss in California's mountain ranges during severe drought from 2012 to 2015 inferred from GPS. J Geophys Res Solid Earth 122(12):10,559-510,585. https://doi.org/10.1002/2017JB014424

Biot MA (1956) Theory of propagation of elastic waves in a fluid-saturated porous solid. II. Higher frequency range. J Acoust Soc Am 28(2):179–191. https://doi.org/10.1121/1.1908241

Biot MA, Willis DG (2021) The elastic coefficients of the theory of consolidation. J Appl Mech 24(4):594–601. https://doi.org/10.1115/1.4011606

Blewitt G, Hammond W (2018) Harnessing the GPS data explosion for interdisciplinary science. Eos 99(2):e2020943118. https://doi.org/10.1073/pnas.2020943118

Blewitt G, Kreemer C, Hammond WC, Goldfarb JM (2013) Terrestrial reference frame NA12 for crustal deformation studies in North America. J Geodyn 72:11–24. https://doi.org/10.1016/j.jog.2013.08.004

Borsa AA, Agnew DC, Cayan DR (2014) Ongoing drought-induced uplift in the western United States. Science 345(6204):1587–1590. https://doi.org/10.1126/science.1260279

Carlson G, Shirzaei M, Werth S, Zhai G, Ojha C (2020) Seasonal and long-term groundwater unloading in the Central Valley modifies crustal stress. J Geophys Res Solid Earth 125(1):e2019JB018490. https://doi.org/10.1029/2019JB018490

Carlson G, Werth S, Shirzaei M (2022) Joint inversion of GNSS and GRACE for terrestrial water storage change in California. J Geophys Res Solid Earth 127(3):e2021JB023135. https://doi.org/10.1029/2021JB023135

Carlson G, Werth S, Shirzaei M (2024) A novel hybrid GNSS, GRACE, and InSAR joint inversion approach to constrain water loss during a record-setting drought in California. Remote Sens Environ 311:114303. https://doi.org/10.1016/j.rse.2024.114303

Crosbie RS, Scanlon BR, Mpelasoka FS, Reedy RC, Gates JB, Zhang L (2013) Potential climate change effects on groundwater recharge in the High Plains Aquifer, USA. Water Resour Res 49(7):3936–3951. https://doi.org/10.1002/wrcr.20292

de Vries JJ, Simmers I (2002) Groundwater recharge: an overview of processes and challenges. Hydrogeol J 10(1):5–17. https://doi.org/10.1007/s10040-001-0171-7

Dill R, Dobslaw H (2013) Numerical simulations of global-scale high-resolution hydrological crustal deformations. J Geophys Res Solid Earth 118(9):5008–5017. https://doi.org/10.1002/jgrb.50353

Farrell W (1972) Deformation of the Earth by surface loads. Rev Geophys 10(3):761–797. https://doi.org/10.1029/RG010i003p00761

Ferreira VG, Montecino HD, Ndehedehe CE, del Rio RA, Cuevas A, de Freitas SR (2019) Determining seasonal displacements of Earth's crust in South America using observations from space-borne geodetic sensors and surface-loading models. Earth Planets Space 71:1–16. https://doi.org/10.1186/s40623-019-1062-2

Galloway DL, Burbey TJ (2011) Review: regional land subsidence accompanying groundwater extraction. Hydrogeol J 19(8):1459–1486. https://doi.org/10.1007/s10040-011-0775-5

Gamelin BL, Feinstein J, Wang J, Bessac J, Yan E, Kotamarthi VR (2022) Projected US drought extremes through the twenty-first

century with vapor pressure deficit. Sci Rep 12(1):8615. https://doi.org/10.1038/s41598-022-12516-7
Golub GH, Heath M, Wahba G (1979) Generalized cross-validation as a method for choosing a good ridge parameter. Technometrics 21(2):215–223. https://doi.org/10.1080/00401706.1979.10489751
Grismer ME (2013) Estimating agricultural deep drainage lag times to groundwater: application to Antelope Valley, California, USA. Hydrol Process 27(3):378–393. https://doi.org/10.1002/hyp.9249
Gualandi A, Liu Z (2021) Variational bayesian independent component analysis for InSAR displacement time-series with application to central California, USA. J Geophys Res Solid Earth 126(4):e2020JB020845. https://doi.org/10.1029/2020JB020845
Gurdak JJ, Roe CD (2010) Review: recharge rates and chemistry beneath playas of the High Plains aquifer, USA. Hydrogeol J 18(8):1747–1772. https://doi.org/10.1007/s10040-010-0672-3
Hammond WC, Burgette RJ, Johnson KM, Blewitt G (2018) Uplift of the Western Transverse Ranges and Ventura Area of Southern California: a four-technique geodetic study combining GPS, InSAR, leveling, and tide gauges. J Geophys Res Solid Earth 123(1):836–858. https://doi.org/10.1002/2017jb014499
Heki K, Jin S (2023) Geodetic study on earth surface loading with GNSS and GRACE. Satell Navig 4(1):1–13. https://doi.org/10.1186/s43020-023-00113-6
Hocking M, Kelly BFJ (2016) Groundwater recharge and time lag measurement through vertosols using impulse response functions. J Hydrol 535:22–35. https://doi.org/10.1016/j.jhydrol.2016.01.042
Humphrey V, Rodell M, Eicker A (2023) Using satellite-based terrestrial water storage data: a review. Surv Geophys. https://doi.org/10.1007/s10712-022-09754-9
Jagucki, M. L., Jurgens, B. C., Burow, K. R., & Eberts, S. M. (2009). Assessing the Vulnerability of Public-Supply Wells to Contamination: Central Valley Aquifer System near Modesto, California (2327–6932).
Jiang W, Yuan P, Chen H, Cai J, Li Z, Chao N, Sneeuw N (2017) Annual variations of monsoon and drought detected by GPS: a case study in Yunnan, China. Sci Rep 7(1):5874. https://doi.org/10.1038/s41598-017-06095-1
Jiang ZS, Hsu YJ, Yuan LG, Huang DF (2021) Monitoring time-varying terrestrial water storage changes using daily GNSS measurements in Yunnan, southwest China. Remote Sens Environ 254:112249. https://doi.org/10.1016/j.rse.2020.112249
Johnson CW, Lau N, Borsa A (2021) An assessment of global positioning system velocity uncertainty in California. Earth Space Sci 8(1):e2020EA001345. https://doi.org/10.1029/2020EA001345
Kang S, Knight R (2023) Isolating the poroelastic response of the groundwater system in InSAR data from the Central Valley of California. Geophys Res Lett 50(9):e2023GL103222. https://doi.org/10.1029/2023GL103222
Langbein J, Bock Y (2004) High-rate real-time GPS network at Parkfield: utility for detecting fault slip and seismic displacements. Geophys Res Lett. https://doi.org/10.1029/2003GL019408
Larochelle S, Chanard K, Fleitout L, Fortin J, Gualandi A, Longuevergne L, Rebischung P, Violette S, Avouac JP (2022) Understanding the geodetic signature of large aquifer systems: example of the Ozark Plateaus in Central United States. J Geophys Res Solid Earth 127(3):e2021JB023097. https://doi.org/10.1029/2021JB023097
Lau N, Borsa AA, Becker TW (2020) Present-day crustal vertical velocity field for the contiguous United States. J Geophys Res Solid Earth 125(10):e2020JB020066. https://doi.org/10.1029/2020JB020066
Lenczuk A, Klos A, Bogusz J (2023) Studying spatio-temporal patterns of vertical displacements caused by groundwater mass changes observed with GPS. Remote Sens Environ 292:113597. https://doi.org/10.1016/j.rse.2023.113597
Li Z, Lu T, He X, Montillet J-P, Tao R (2023) An improved cyclic multi model-eXtreme gradient boosting (CMM-XGBoost) forecasting algorithm on the GNSS vertical time series. Adv Space Res 71(1):912–935. https://doi.org/10.1016/j.asr.2022.08.038
Loomis B, Luthcke S, Sabaka T (2019) Regularization and error characterization of GRACE mascons. J Geod. https://doi.org/10.1007/s00190-019-01252-y
Loomis BD, Rachlin KE, Wiese DN, Landerer FW, Luthcke SB (2020) Replacing GRACE/GRACE-FO c30 with satellite laser ranging: impacts on Antarctic Ice Sheet mass change. Geophys Res Lett 47(3):e2019GL085488. https://doi.org/10.1029/2019GL085488
Martens, H. R., Argus, D. F., Norberg, C., Blewitt, G., Herring, T. A., Moore, A. W., Hammond, W. C., & Kreemer, C. (2020). Atmospheric pressure loading in GPS positions: dependency on GPS processing methods and effect on assessment of seasonal deformation in the contiguous USA and Alaska. *Journal of Geodesy*, *94*(12). https://doi.org/10.1007/s00190-020-01445-w
Masson-Delmotte, V., Zhai, P., Pirani, A., Connors, S. L., Péan, C., Berger, S., Caud, N., Chen, Y., Goldfarb, L., & Gomis, M. (2021). Climate change 2021: the physical science basis. *Contribution of working group I to the sixth assessment report of the intergovernmental panel on climate change*,*2*.
Müller Schmied H, Cáceres D, Eisner S, Flörke M, Herbert C, Niemann C, Peiris TA, Popat E, Portmann FT, Reinecke R, Schumacher M, Shadkam S, Telteu CE, Trautmann T, Döll P (2021) The global water resources and use model WaterGAP v2.2d: model description and evaluation. Geosci Model Dev 14(2):1037–1079. https://doi.org/10.5194/gmd-14-1037-2021
Niu GY, Yang ZL, Mitchell KE, Chen F, Ek MB, Barlage M, Kumar A, Manning K, Niyogi D, Rosero E (2011) The community Noah land surface model with multiparameterization options (Noah-MP): 1. model description and evaluation with local-scale measurements. J Geophys Res. https://doi.org/10.1029/2010JD015139
Ojha C, Shirzaei M, Werth S, Argus DF, Farr TG (2018) Sustained groundwater loss in California's Central Valley exacerbated by intense drought periods. Water Resour Res 54(7):4449–4460. https://doi.org/10.1029/2017wr022250
Overacker J, Hammond WC, Blewitt G, Kreemer C (2022) Vertical land motion of the High Plains Aquifer Region of the United States: effect of aquifer confinement style, climate variability, and anthropogenic activity. Water Resour Res 58(6):e2021WR031635. https://doi.org/10.1029/2021WR031635
Peltier WR, Argus D, Drummond R (2015) Space geodesy constrains ice age terminal deglaciation: the global ICE-6G_C (VM5a) model. J Geophys Res Solid Earth 120(1):450–487. https://doi.org/10.1002/2014JB011176
Peltier W, Argus DF, Drummond R (2018) Comment on "An assessment of the ICE-6G_C (VM5a) glacial isostatic adjustment model" by Purcell et al. J Geophys Res Solid Earth 123(2):2019–2028. https://doi.org/10.1002/2016JB013844
Petit, G., & Luzum, B. (2010). IERS technical note 36 (179 pp.). Frankfurt, Germany: Bundesamts für Kartogr. und Geod.
Razeghi M, Tregoning P, Shirzaei M, Ghobadi-Far K, McClusky S, Renzullo L (2022) Characterization of changes in groundwater storage in the Lachlan Catchment, Australia, derived from observations of surface deformation and groundwater level data. J Geophys Res Solid Earth 127(12):e2022JB024669. https://doi.org/10.1029/2022JB024669
Renu S, Pramada S (2023) Use of grace and in-situ data to characterize groundwater status along the coast of Kerala. J Earth Syst Sci 132(3):1–15. https://doi.org/10.1007/s12040-023-02150-w
Riel B, Simons M, Ponti D, Agram P, Jolivet R (2018) Quantifying ground deformation in the Los Angeles and Santa Ana Coastal Basins due to groundwater withdrawal. Water Resour Res 54(5):3557–3582. https://doi.org/10.1029/2017wr021978

Rodriguez-Solano C, Hugentobler U, Steigenberger P, Bloßfeld M, Fritsche M (2014) Reducing the draconitic errors in GNSS geodetic products. J Geod 88(6):559–574. https://doi.org/10.1007/s00190-014-0704-1

Save H, Bettadpur S, Tapley BD (2016) High-resolution CSR GRACE RL05 mascons. J Geophys Res Solid Earth 121(10):7547–7569. https://doi.org/10.1002/2016JB013007

Scanlon BR, Faunt CC, Longuevergne L, Reedy RC, Alley WM, McGuire VL, McMahon PB (2012) Groundwater depletion and sustainability of irrigation in the US High Plains and Central Valley. Proc Natl Acad Sci U S A 109(24):9320–9325. https://doi.org/10.1073/pnas.1200311109

Shirzaei M, Ojha C, Werth S, Carlson G, Vivoni ER (2019) Comment on "Short-lived pause in Central California subsidence after heavy winter precipitation of 2017" by KD Murray and RB Lohman. Sci Adv 5(6):eaav8038. https://doi.org/10.1126/sciadv.aar8144

Smith RG, Knight R, Chen J, Reeves JA, Zebker HA, Farr T, Liu Z (2017) Estimating the permanent loss of groundwater storage in the southern San Joaquin Valley, California. Water Resour Res 53(3):2133–2148. https://doi.org/10.1002/2016wr019861

Sun Y, Riva R, Ditmar P (2016) Optimizing estimates of annual variations and trends in geocenter motion and from a combination of GRACE data and geophysical models. J Geophys Res-Solid Earth 121(11):8352–8370. https://doi.org/10.1002/2016jb013073

Swenson S, Chambers D, Wahr J (2008) Estimating geocenter variations from a combination of GRACE and ocean model output. J Geophys Res Solid Earth 113(B8). https://doi.org/10.1029/2007JB005338

Turkeltaub T, Kurtzman D, Bel G, Dahan O (2015) Examination of groundwater recharge with a calibrated/validated flow model of the deep vadose zone. J Hydrol 522:618–627. https://doi.org/10.1016/j.jhydrol.2015.01.026

Valley, S. (2009). Groundwater availability of the Central Valley aquifer, California. US Geological Survey professional paper.

Vasco DW, Kim KH, Farr TG, Reager JT, Bekaert D, Sangha SS, Rutqvist J, Beaudoing HK (2022) Using Sentinel-1 and GRACE satellite data to monitor the hydrological variations within the Tulare Basin, California. Sci Rep 12(1):3867. https://doi.org/10.1038/s41598-022-07650-1

Vereecken H, Amelung W, Bauke SL, Bogena H, Brüggemann N, Montzka C, Vanderborght J, Bechtold M, Blöschl G, Carminati A (2022) Soil hydrology in the Earth system. Nat Rev Earth & Environ 3(9):573–587. https://doi.org/10.1038/s43017-022-00324-6

Wahr J, Molenaar M, Bryan F (1998) Time variability of the Earth's gravity field: hydrological and oceanic effects and their possible detection using GRACE. J Geophys Res Solid Earth 103(B12):30205–30229. https://doi.org/10.1029/98jb02844

Wang L, Chen C, Du J, Wang T (2017) Detecting seasonal and long-term vertical displacement in the North China Plain using GRACE and GPS. Hydrol Earth Syst Sci 21(6):2905–2922. https://doi.org/10.5194/hess-21-2905-2017

Wang L, Chen C, Ma X, Fu Z, Zheng Y, Peng Z (2020) Evaluation of GRACE mascon solutions using in-situ geodetic data: the case of hydrologic-induced crust displacement in the Yangtze River Basin. Sci Total Environ 707:135606. https://doi.org/10.1016/j.scitotenv.2019.135606

White AM, Gardner WP, Borsa AA, Argus DF, Martens HR (2022) A review of GNSS/GPS in hydrogeodesy: hydrologic loading applications and their implications for water resource research. Water Resour Res 58(7):e2022WR032078. https://doi.org/10.1029/2022WR032078

Wiese DN, Landerer FW, Watkins MM (2016) Quantifying and reducing leakage errors in the JPL RL05M GRACE mascon solution. Water Resour Res 52(9):7490–7502. https://doi.org/10.1002/2016WR019344

Wiese, D., Yuan, D., Boening, C., Landerer, F., & Watkins, M. (2018). JPL GRACE mascon ocean, ice, and hydrology equivalent water height release 06 coastal resolution improvement (CRI) filtered version 1.0. DAAC: Pasadena, CA, USA.

Wilson AM, Gorelick S (1996) The effects of pulsed pumping on land subsidence in the Santa Clara Valley, California. J Hydrol 174(3–4):375–396. https://doi.org/10.1016/0022-1694(95)02722-X

Xu XQ, Dong DN, Fang M, Zhou YH, Wei N, Zhou F (2017) Contributions of thermoelastic deformation to seasonal variations in GPS station position. GPS Solut 21(3):1265–1274. https://doi.org/10.1007/s10291-017-0609-6

Yang ZY, Wang K, Yuan Y, Huang JT, Chen ZJ, Li C (2019) Non-negligible lag of groundwater infiltration recharge: a case in Mu Us Sandy Land, China. Water 11(3):561. https://doi.org/10.3390/w11030561

Zhang M, Yuan X (2020) Rapid reduction in ecosystem productivity caused by flash droughts based on decade-long FLUXNET observations. Hydrol Earth Syst Sci 24(11):5579–5593. https://doi.org/hess-24-5579-2020

Zhang S, Luo B, Ben-Zion Y, Lumley DE, Zhu H (2023) Monitoring terrestrial water storage, drought and seasonal changes in central Oklahoma with ambient seismic noise. Geophys Res Lett 50(17):e2023GL103419. https://doi.org/10.1029/2023GL103419

Zhao M, Liu Y, Konings AG (2022) Evapotranspiration frequently increases during droughts. Nat Clim Chang 12(11):1024–1030. https://doi.org/10.1038/s41558-022-01505-3

Zheng S, Heki K, Zhang ZZ, Tokui Y, Yan HM (2023) Interference of ocean and land mass changes in seasonal crustal deformation of coastal stations: a case study in northern Australia. Earth Planet Sci Lett 614:118212. https://doi.org/10.1016/j.epsl.2023.118212

Zhong B, Li X, Chen J, Li Q, Liu T (2020) Surface mass variations from GPS and GRACE/GFO: a case study in southwest China. Remote Sens 12(11):1835. https://doi.org/10.3390/rs12111835

Zhu H, Chen KJ, Hu SQ, Wang J, Wang ZY, Li JF, Liu JG (2024) A novel GNSS and precipitation-based integrated drought characterization framework incorporating both meteorological and hydrological indicators. Remote Sens Environ 311:114261. https://doi.org/10.1016/j.rse.2024.114261